Sonic hedgehog-dependent recruitment of GABAergic interneurons into the developing visual thalamus

Rachana Deven Somaiya[1,2], Katelyn Stebbins[1,2,3], Ellen C. Gingrich[4,5], Hehuang Xie[6,7,8,9], John N. Campbell[10,11], A. Denise R. Garcia[4,5], Michael A. Fox[1,7,12,13*]

1. Center for Neurobiology Research, Fralin Biomedical Research Institute at Virginia Tech Carilion, Roanoke, Virginia, 24016, USA
2. Graduate Program in Translational Biology, Medicine, and Health, Virginia Tech, Blacksburg, Virginia, 24061, USA
3. Virginia Tech Carilion School of Medicine, Roanoke, 24016, USA
4. Department of Biology, Drexel University, Philadelphia, Pennsylvania, 19104, USA
5. Department of Neurobiology and Anatomy, Drexel University College of Medicine, Philadelphia, Pennsylvania, 19104, USA
6. Fralin Life Sciences Institute at Virginia Tech, Blacksburg, VA, 24061, USA
7. School of Neuroscience, College of Science, Virginia Tech, Blacksburg, Virginia, 24061, USA
8. Genetics, Bioinformatics and Computational Biology Program, Virginia Tech, Blacksburg, VA 24061, USA
9. Department of Biomedical Sciences and Pathobiology, Virginia-Maryland College of Veterinary Medicine, Blacksburg, Virginia, 24061, USA
10. Department of Biology, University of Virginia, Charlottesville, VA 22904 USA
11. Neuroscience Graduate Program, University of Virginia, Charlottesville, VA 22904 USA
12. Department of Biological Sciences, College of Science, Virginia Tech, Blacksburg, Virginia, 24061, USA
13. Department of Pediatrics, Virginia Tech Carilion School of Medicine, Roanoke, Virginia, 24016, USA

* Correspondence: mafox1@vt.edu

Abstract:

Axons of retinal ganglion cells (RGCs) play critical roles in the development of inhibitory circuits in visual thalamus. We previously reported that RGC axons signal astrocytes to induce the expression of fibroblast growth factor 15 (FGF15), a motogen required for GABAergic interneuron migration into visual thalamus. However, how retinal axons induce thalamic astrocytes to generate *Fgf15* and influence interneuron migration remains unknown. Here, we demonstrate that impairing RGC activity had little impact on interneuron recruitment into mouse visual thalamus. Instead, our data show that retinal-derived sonic hedgehog (SHH) is essential for interneuron recruitment. Specifically, we show that thalamus-projecting RGCs express SHH and thalamic astrocytes generate downstream components of SHH signaling. Deletion of RGC-derived SHH leads to a significant decrease in *Fgf15* expression, as well as in the percentage of interneurons recruited into visual thalamus. Thus, our findings identify a morphogen-dependent neuron-astrocyte signaling mechanism essential for the migration of thalamic interneurons.

Keywords

lateral geniculate nucleus, sonic hedgehog, astrocytes, interneurons, retinal ganglion cells, fibroblast growth factors

Acknowledgments

This work was supported by National Institutes of Health grants EY021222 (M.A.F.), EY030568 (M.A.F.), EY033528 (M.A.F. and J.N.C), HL153916 (J.N.C) and American Diabetes Association Pathway to Stop Diabetes Award 1-18-INI-14 (J.N.C.). We are grateful to the members of the M.A.F. lab for scientific discussion and comments on the manuscript. We thank Dr. Stefanie Robel for providing *Aldh1l1-EGFP* mice, Dr. Steven W. Wang for providing *Atoh7*$^{-/-}$ mice, and Dr. Anton Maximov for providing *Rosa26*$^{floxstop\text{-}TeNT}$ mice. The authors also thank Dr. Karthik Shekhar (University of California, Berkeley) for input on bioinformatics approaches.

Declaration of interests: The authors declare no competing interests.

INTRODUCTION

The retina receives light-derived signals from our visual environment and transmits those signals to several dozen regions of the brain via axons of retinal ganglion cells (RGCs). In rodents, one of the brain regions densely innervated by RGC axons is the visual thalamus, which includes several retinorecipient nuclei, such as the dorsal lateral geniculate nucleus (dLGN), intergeniculate leaflet (IGL), and ventral lateral geniculate nucleus (vLGN). Despite being adjacent, these nuclei have diverse roles in visual processing, with the dLGN being important for image-forming visual functions, and the vLGN and IGL contributing more to non-image-forming visual functions (such as visuomotor functions, circadian photoentrainment, and mood regulation) (Fratzl et al., 2021; Guido, 2018; Huang et al., 2019; Monavarfeshani et al., 2017; Salay and Huberman, 2021). Not surprisingly based on these diverse functions, the principal neurons and their connectivity differs greatly between dLGN and vLGN/IGL (Krahe et al., 2011; Sabbagh et al., 2018, 2021). In fact, while the most abundant neurons in dLGN are glutamatergic thalamocortical relay cells, most neurons in vLGN are GABAergic and appear to represent a heterogeneous group of cell types with distinct morphologies, projections, and functions (Ciftcioglu et al., 2020; Crombie and Busse, 2021; Harrington, 1997; Yuge et al., 2011).

Despite these differences, there are some similarities in the cell types of dLGN and vLGN, including the presence and distribution of local interneurons (Arcelli et al., 1997; Evangelio et al., 2018; Jaubert-Miazza et al., 2005). In fact, a shared mechanism appears to exist that contributes to the recruitment and integration of these GABAergic neurons into both dLGN and vLGN (Golding et al., 2014; Su et al., 2020). Specifically, the recruitment of migrating interneurons into the perinatal dLGN and vLGN requires the innervation of these regions by RGC axons. Our previous work identified a mechanism underlying this process (Su et al., 2020): we reported that the expression of migratory cue fibroblast growth factor 15 (FGF15) by thalamic astrocytes is dependent on retinal inputs and the loss of this FGF leads to a reduction in the number of GABAergic interneurons in visual thalamus. We observed that the decrease in the number of GABAergic interneurons in the absence of FGF15 is not due to an increase in programmed cell death. Instead, these cells are misrouted into regions adjacent to the dorsal thalamus, specifically affecting their recruitment into dLGN and vLGN. However, it remains unclear how exactly retinal axons instruct astrocytes to generate FGF15 and to facilitate interneuron recruitment into visual thalamus.

Here, we sought to determine the role of retinal activity and/or axon-derived factors in the FGF15-dependent interneuron migration into the developing visual thalamus. Our data shows that impairing the activity of RGCs by genetically expressing tetanus toxin disrupts eye-specific segregation in dLGN and causes visual deficits in mice; however, it had little impact on interneuron recruitment into visual thalamus. Instead, we discovered that retinal-derived sonic hedgehog (SHH) is necessary for interneuron recruitment. Not only do RGCs express SHH in the perinatal retina, but also astrocytes in the developing visual thalamus express several downstream molecules involved in the canonical SHH signaling pathway, such as *Ptch1*, *Smo*, and *Gli1*. Conditional deletion of SHH from RGCs led to decrease in *Fgf15* expression and deficits in interneuron migration into visual thalamus. Thus, our findings demonstrate a novel activity-independent and SHH-dependent molecular mechanism for RGC axons to orchestrate thalamic interneuron migration.

RESULTS

Sonic Hedgehog (SHH), but not retinal activity, is critical for interneuron recruitment into visual thalamus

Using *Atoh7*$^{-/-}$ (also called *Math5*$^{-/-}$) mutant mice, which lack RGC inputs to visual thalamus (Figure 1a), we previously reported a significant reduction in the number of interneurons in visual thalamus (Su et al., 2020). Here, we demonstrate this loss using *in situ* hybridization (ISH) for *Gad1* mRNA, which encodes for glutamic acid decarboxylase 67 (GAD67), an enzyme required for the production of GABA. This confirmed significant reduction in *Gad1*$^{+}$ neurons in both dLGN and vLGN (Figures 1a-c). It is important to highlight that the reduction in *Gad1*$^{+}$ cells in *Atoh7*$^{-/-}$ vLGN is less striking than in dLGN, since most *Gad1*$^{+}$ cells in vLGN are principal projection cells and not local interneurons.

Although the expression of FGF15 in visual thalamus is dependent on retinal inputs (Su et al., 2020, Figure 1—figure supplement 1a), it remains unclear whether this is due to neuronal activity or developmentally regulated factors released by RGC axons. Here, we set out to distinguish between these possibilities. First, we tested whether retinal activity was necessary for the interneuron recruitment into visual thalamus. To impair neuronal activity from RGCs, we took advantage of a transgenic Cre-inducible system to express Tetanus toxin (TeNT) in RGCs (*Rosa26*$^{floxstop\text{-}TeNT}$). TeNT is a protease that cleaves the vesicular SNARE Synaptobrevin2/VAMP2 (Syb2), which is required for the exocytosis of

neurotransmitters (Link et al., 1992; Schoch et al., 2001). We crossed mice carrying the *Rosa26*$^{floxstop\text{-}TeNT}$ allele with *Calb2*^{Cre} mice, in which most, if not all, RGCs express Cre recombinase (Kerr et al., 2019; Sando et al., 2017; Zhang et al., 2008) and widespread expression of Cre occurs in the GCL of the retina as early as P0 (Figure 1d and Figure 1—figure supplement 2a). Our selection of *Calb2*^{Cre} over *Slc17a6*^{Cre} (also called vesicular glutamate transporter 2, *Vglut2*^{Cre}), another widely used transgenic line to target RGCs (Wang et al., 2020), was based on the relatively low expression of *Calb2* mRNA in dLGN (Ahmadlou et al., 2018) as compared to *Slc17a6* (Land et al., 2004).

Studies that have employed *Rosa26*$^{floxstop\text{-}TeNT}$ to block neural activity have confirmed the suppression of neurotransmitter release by observing a loss of Syb2 in Cre-expressing cells (Sando et al., 2017). However, retinal inputs account for only 5-10% of the total synapses onto a dLGN relay cell (Bickford et al., 2010; Van Horn et al., 2000; Sherman and Guillery, 2002), making it difficult to detect significant changes in just a small fraction of the synapses in visual thalamus. Therefore, we sought other approaches to confirm impaired retinogeniculate (RG) neuronal activity in *Rosa26*$^{floxstop\text{-}TeNT}$*;Calb2*^{Cre}. RGC activity during perinatal development is critical for eye-specific segregation of retinal axons (Huberman et al., 2003; Penn et al., 1998; Pfeiffenberger et al., 2005), therefore, we assessed eye-specific RGC projections in *Rosa26*$^{floxstop\text{-}TeNT}$*;Calb2*^{Cre} mice. Retinal terminals were labeled by intraocular injection of different fluorescently conjugated CTB into each eye at P12-P20. In *Rosa26*$^{floxstop\text{-}TeNT}$*;Calb2*^{Cre} mice, we observed a significant increase in the area occupied by inputs from both eyes, a hallmark of impaired activity-dependent RG refinement (Figure 1—figure supplement 2d-e). Blocking retinal activity in these mice should also significantly impact visual behaviors, therefore, we also tested responses to a “looming stimulus” (Koehler et al., 2019). When presented with dark looming stimuli, control mice displayed an escape response, running to a shelter within the arena. In contrast, *Rosa26*$^{floxstop\text{-}TeNT}$*;Calb2*^{Cre} mutants had impaired escape responses, indicating deficits in their ability to identify visual stimuli, although it is important to note that these responses were not as impaired as observed in *Atoh7*$^{-/-}$ mutants (Figure 1—figure supplement 2b and c). Together, these sets of both results suggest that there is a significant impairment in glutamate release by retinal axons in *Rosa26*$^{floxstop\text{-}TeNT}$*;Calb2*^{Cre} mice, confirming that this mutant line can be used to study the role of retinal activity in the developing brain.

Using riboprobes against *Gad1*, we performed ISH to detect changes in percentage of interneurons in the visual thalamus of *Rosa26*$^{floxstop\text{-}TeNT}$*;Calb2*^{Cre} mice. Surprisingly, in dLGN and vLGN, we did not observe a significant difference in the percentage of *Gad1*-expressing cells between the controls and mutants, revealing that decreasing retinal activity, or at least glutamate release by RGCs, had little impact on the recruitment of interneurons into visual thalamus (Figure 1e and f).

Since retinal activity did not appear critical for interneuron recruitment into visual thalamus, we next investigated whether RGCs released factors beyond neurotransmitters, which could influence migration of thalamic interneurons. SHH signaling widely regulates FGF15 expression in the embryonic brain (Ishibashi and McMahon, 2002; Martinez-Ferre et al., 2016; Saitsu et al., 2005) and RGCs have been reported to generate and secrete SHH (Dakubo et al., 2008; Peng et al., 2018; Traiffort et al., 2001; Wallace and Raff, 1999), suggesting that SHH might regulate FGF15 expression and interneuron migration into visual thalamus. To test whether this was the case, we utilized a conditional allele of *Shh*$^{fl/fl}$ and crossed it with *Nes*^{Cre}, in which there is early expression of Cre in neuronal and glial progenitors (Tronche et al., 1999) (Figure 1g). As previously reported, *Shh*$^{fl/fl}$*Nes*^{Cre} mutants survive gestation, however, die by P18 (Machold et al., 2003; Xu et al., 2005). In dLGN and vLGN of these mutants, we observed a significant and dramatic decrease in the percentage of *Gad1*-expressing neurons (Figure 1h and i). Furthermore, loss of SHH signaling in *Shh*$^{fl/fl}$*Nes*^{Cre} mice resulted in a reduction in *Fgf15* expression, similar to what was observed in mice lacking retinal inputs (Figure 1—figure supplement 1b and c). Thus, SHH signaling appears critical for both thalamic *Fgf15* expression and the recruitment of interneurons into dLGN and vLGN.

Astrocytic expression of SHH signaling components

Activation of the SHH pathway is initiated when extracellular SHH binds to its canonical receptor, Patched-1 (PTCH1), present on target cells. This binding leads to the release of PTCH1-mediated inhibition of the membrane-spanning receptor, Smoothened (SMO), thereby allowing it to activate glioma-associated oncogene (GLI) transcription factors. Since our previous studies revealed that FGF15 is specifically generated by thalamic astrocytes during perinatal development (Su et al., 2020), we asked whether these astrocytes express components of the SHH signaling.

Using previously generated RNAseq datasets, we first assessed the expression profiles of several SHH signaling genes in the developing mouse dLGN and vLGN (Monavarfeshani et al., 2018). Analysis of this data showed that three canonical SHH signaling components, *Ptch1*, *Smo*, and *Gli1*, are expressed in visual thalamus at P3 (Figure 2a), when *Fgf15* expression is high in this region (Su et al., 2020). To determine whether astrocytes express these components in visual thalamus, we undertook several approaches. First, we utilized *Rosa26*^{tdT}*;Gli1*^{CreER} mice whereby tamoxifen administration leads to Cre-mediated recombination of the tdT fluorescent protein in *Gli1*-expressing cells (Hill et al., 2019). Thalamic slices from P7 *Rosa26*^{tdT}*;Gli1*^{CreER} showed the presence of *Gli1-tdT*$^{+}$ cells in both dLGN and vLGN (Figure 2b). Immunostaining for S100ß, a commonly used marker for astrocytes, revealed S100ß expression in *Gli1-tdT*$^{+}$ cells, suggesting that these astrocytes generate *Gli1* (Figure 2c-d). However, we recently reported that S100ß IHC also labels a small population of microglia in visual thalamus (Somaiya et al., 2021), therefore, we confirmed that *tdT*$^{+}$ cells were astrocytes by ISH for *Gja1*, the gene encoding Connexin 43. In fact, we observed that *Gja1* mRNA was present in all *Gli1-tdT*$^{+}$ cells, suggesting expression of this transcription factor was specific to astrocytes in visual thalamus (Figure 2e-f).

We next examined the expression of *Ptch1* and *Smo* in thalamic astrocytes. For this, we performed ISH in *Aldh1l1-GFP* mice in which most thalamic astrocytes are labelled with GFP (Somaiya et al., 2021). ISH with riboprobes against *Ptch1* and *Smo* revealed that a high percentage of *Aldh1l1-GFP*$^{+}$ astrocytes express these genes in P3 dLGN and vLGN (Figures 2g-j). Together, these data demonstrate that astrocytes in perinatal visual thalamus have the cellular machinery to respond to SHH.

SHH is generated by RGCs in the developing perinatal retina

Several studies have shown that RGCs generate and release SHH (Dakubo et al., 2008; Peng et al., 2018; Su et al., 2020; Traiffort et al., 2001; Wallace and Raff, 1999), therefore, we next asked whether they also express SHH at times corresponding to FGF15 expression in the visual thalamus. At P3, not only is *Shh* mRNA expression restricted to the GCL of the retina, but it is expressed by CALB2^{+} RGCs (Figure 3a-b). Since at least 40 transcriptionally distinct types of RGCs exist in the mouse retina (Tran et al., 2019), we sought to identify whether all RGCs generate *Shh* mRNA (which looked to be the case based on ISH, Figure 3a) or whether specific RGC subtypes generate this morphogen in the perinatal retina. Rheaume et al. recently performed a comprehensive transcriptomic analysis of all mouse RGC subtypes at P5, therefore, we reanalyzed their publicly available single-cell RNAseq dataset to answer this question (Rheaume et al., 2018). Two important observations were made through this analysis: 1) All RGC subtypes express high levels of *Calb2*, confirming the reliability of targeting this molecule to study RGCs (Kerr et al., 2019); 2) At least 39 out of 41 RGC subtypes express *Shh* mRNA (Figure 3c). These results suggested that RGCs in the developing postnatal retina express SHH, which can potentially influence the role of thalamic astrocytes.

RGC-derived SHH is required for FGF15 expression and interneuron recruitment into visual thalamus

Previous studies have shown that RGC-derived SHH protein travels all the way to the optic nerve (Wallace and Raff, 1999) and can even be detected in retinorecipient brain areas (Traiffort et al., 2001). To report active SHH signaling in developing visual thalamus, we tested for the presence of *Gli1.* Loss of SHH has been observed to abrogate *Gli1* expression, suggesting that it can be used as a proxy for SHH protein (Garcia et al., 2010). Here, staining for βGal in P3 *Gli1*$^{nlacZ/+}$ mice demonstrated that when thalamic *Fgf15* expression is high and interneuron migration occurs, there is indeed active SHH signaling in dLGN and vLGN (Figure 3—figure supplement 1).

To assess the role of SHH signaling in the developing visual thalamus, we first sought approaches to delete *Ptch1* or *Smo* from astrocytes. However, we could not find an appropriate transgenic line that would achieve sufficient Cre recombination to delete these genes exclusively in astrocytes during early development. For instance, *Gfap-cre* shows only sparse Cre expression in visual thalamus before eye-opening (Somaiya et al., 2021); *Aldh1l1*^{Cre} displays Cre expression not only in astrocytes but also in some oligodendrocytes during early development (Tien et al., 2012); and *Aldh1l1*$^{Cre/ERT2}$ could potentially cause significant challenges to the process of natural birth due to tamoxifen administration to pregnant mice (Lizen et al., 2015). Therefore, to circumvent these issues, we instead assessed the role of SHH signaling in the developing visual thalamus by crossing conditional allele *Shh*$^{fl/fl}$ with *Calb2*^{Cre} mice. Multiple reasons led us to choose *Calb2*^{Cre} mice to target RGC-derived SHH: 1) *Shh* and *Calb2* are co-expressed in RGC subtypes (Figure 3c); 2) RGCs show no to very low expression of *Calb2* before E16 (Shekhar et al., 2022), suggesting that *Shh*$^{fl/fl}$*;Calb2*^{Cre} mutant mice will retain other known Shh functions (Wang et al., 2005) in early embryonic retina (Figure 3d); 3) Our previous

studies have demonstrated significant reduction in gene expression specifically in RGCs using the *Calb2*^{Cre} driver line (Kerr et al., 2019); 4) We previously reported that CALB2^{+} cells are largely absent from the neonatal and postnatal dLGN and are only sparsely distributed in vLGN at these ages (Su et al., 2011). Here, we add to these points by showing only a limited number of CALB2^{+} cells are present in the thalamic and tectal progenitor zones that are thought to give rise to these sets of migrating interneurons (Golding et al., 2014; Jager et al., 2016)(Figure 3—figure supplement 2). Therefore, using *Calb2*^{Cre} mice potentially minimizes bias caused by deletion of SHH from these regions as seen in *Shh*$^{fl/fl}$*Nes*^{Cre} mutants.

Shh$^{fl/fl}$*;Calb2*^{Cre} mutant mice are viable, fertile, and indistinguishable from littermate controls. qRT-PCR analysis confirmed a significant decrease in *Shh* mRNA in the retina of these mutants (Figure 3e). Intraocular CTB injections showed that RGC axons from both eyes in *Shh*$^{fl/fl}$*;Calb2*^{Cre} mice are capable of innervating dLGN and form normal appearing eye-specific projections in this region (Figure 4). The appropriate targeting of retinal axons into visual thalamus of *Shh*$^{fl/fl}$*;Calb2*^{Cre} mice suggests that any deficits we observe in these mutants is likely not a secondary consequence of dysinnervation in these mutants (such as the absence of any other axon-derived molecules).

Based on this reduction in RGC-derived SHH, we investigated if RGC-derived SHH is necessary for astrocytic expression of FGF15 in the developing visual thalamus. ISH analysis demonstrated a significant reduction of *Fgf15*$^{+}$ cells in the dLGN and vLGN of P3 *Shh*$^{fl/fl}$*;Calb2*^{Cre} mutants (Figure 5a and b). These results resembled the reduced number of *Fgf15*$^{+}$ cells in both the *Atoh7*$^{-/-}$ visual thalamus and *Shh*$^{fl/fl}$*Nes*^{Cre} visual thalamus. Next, to determine if the changes in *Fgf15* expression are the result of a decrease in astrocyte numbers, we used an astrocyte-specific mRNA we previously found to be expressed by all astrocytes in the developing visual thalamus – fibroblast growth factor receptor 3 (*Fgfr3*) mRNA (Somaiya et al., 2021). It is important to point out for clarity that FGFR3 is not a major receptor for FGF15 (Ornitz and Itoh, 2015). ISH analysis showed no significant difference in the distribution of *Fgfr3*-expressing cells between the controls and mutants (Figure 5c and d), suggesting that loss of RGC-derived SHH does not the impact number of astrocytes in developing dLGN and vLGN. These results demonstrate that SHH signaling from RGCs is not only necessary for astrocytic expression of *Fgf15* in visual thalamus but that RGCs are the primary source of SHH to drive *Fgf15* expression in thalamic astrocytes.

Given the importance of FGF15 from our studies, we subsequently examined the effect of loss of RGC-derived SHH on thalamic interneurons. We first assessed changes in interneuron recruitment after the first week of postnatal development, at the time when these cells have fully migrated into dLGN and vLGN (Su et al., 2020). Our ISH data revealed that there was significant reduction in the percentage of *Gad1*-expressing cells in dLGN and vLGN of *Shh*$^{fl/fl}$*;Calb2*^{Cre} mice at P7 (Figure 6a and b). It is possible, however, that the absence of RGC-derived SHH does not completely halt thalamic interneuron recruitment, but rather delays this migration process. Thus, we also investigated changes in the number of interneurons in adult *Shh*$^{fl/fl}$*;Calb2*^{Cre} mice. Indeed, our data revealed a persistent, significant decrease in the percentage of *Gad1*-expressing cells in dLGN and vLGN of adult mutants (Figure 6c and d), similar to what we have previously reported to occur in the visual thalamus of *Fgf15*$^{-/-}$ mutants (Su et al., 2020). Overall, our findings highlight the dependence of astrocytic *Fgf15* expression and recruitment of GABAergic interneurons into visual thalamus on the SHH signaling from retina.

DISCUSSION

The development of sensory neuronal circuits in many brain structures is coordinated by the arrival of sensory inputs, neuronal activity, and sensory experience (C. Brunjes, 1994; Katz and Shatz, 1996; Nithianantharajah and Hannan, 2006; Sanes and Lichtman, 2001). Here, we focused on the visual system where a growing body of evidence highlights critical roles for RGC axons and retinal activity in orchestrating thalamic development (Brooks et al., 2013; Charalambakis et al., 2019; Golding et al., 2014; Grant et al., 2016; He et al., 2019; Sabbagh et al., 2018; Seabrook et al., 2013). As one example, we previously reported that the retinal inputs signal through thalamic astrocytes to facilitate the recruitment of interneurons into dLGN and vLGN (Su et al., 2020). Specifically, thalamic astrocytes generate the motogen FGF15, which in contrast to other FGFs has reduced heparin-binding affinity (Ornitz and Itoh, 2015) making it an ideal guidance cue for long-distance migration of interneurons (Golding et al., 2014; Jager et al., 2016, 2021). In this study, we uncovered the molecular mechanism by which RGC axons signal to thalamic astrocytes to influence FGF15 expression. We show that this process is independent of RGC activity, but reliant upon SHH derived from the retina. The results highlight a SHH-dependent axo-glial-neuronal signaling mechanism important for thalamic development.

SHH as an intermediary between RGCs and thalamic astrocytes for interneuron migration

SHH signaling has well established roles in regulating morphogenesis, cell differentiation, and cell proliferation (Garcia et al., 2018; Ishibashi and McMahon, 2002; Komada et al., 2008a; Marigo et al., 1996). In the embryonic retina, local expression of SHH is critical for promoting and maintaining the proliferation of retinal precursor cells (Jensen and Wallace, 1997; Wang et al., 2005). However, here we observed that *Shh* expression is largely confined to RGCs at perinatal ages. RGC-derived SHH protein has been shown to be anterogradely transported along axons, where it maintains the proliferative capacity of astrocytes in the optic nerve (Dakubo et al., 2008; Wallace and Raff, 1999) and acts as cue to guide eye-specific axon segregation at the optic chiasm (Peng et al., 2018). Radiolabeling experiments have reported the presence of retina-derived SHH as far as the superior colliculus (Traiffort et al., 2001), a midbrain retinorecipient region, suggesting previously unexplored roles for RGC-derived SHH likely exist beyond the optic nerve and chiasm.

In the current study, we discovered that retinal-derived SHH plays important roles in the recruitment of interneurons into visual thalamus, a major RGC target site in the brain. These results are in line with several recent studies with showing that neuron-derived SHH directly acts on astrocytes residing in the target regions of their axonal projections (Garcia et al., 2010; Hill et al., 2019). We show that astrocytes in visual thalamus generate several downstream components of SHH signaling and that RGC-derived SHH is critical for astrocytic *Fgf15* expression in visual thalamus. While FGF15 expression has been shown to be dependent on local SHH signaling in the embryonic brain (Ishibashi and McMahon, 2002; Kim et al., 2018; Komada et al., 2008b; Saitsu et al., 2005; Yabut et al., 2019), this is the first study to provide evidence for long-distance SHH signaling to regulate the expression of astrocyte-derived FGF15.

The loss of astrocyte-derived FGF15 in $Shh^{fl/fl};Calb2^{Cre}$ mutants results in a significant loss of $Gad1^{+}$ interneurons in both dLGN and vLGN. However, it does not result in an absence of these GABAergic neurons. In other brain regions, the loss of SHH signaling has been observed to dramatically affect specific subtypes of GABAergic neurons, such as interneurons that express parvalbumin (Pvalb) or Somatostatin (Sst) (Ihrie et al., 2011; Xu et al., 2005), which may explain the partial loss of $Gad1^{+}$ cells in the visual thalamus of $Shh^{fl/fl};Calb2^{Cre}$ mutants. In dLGN, transcriptional, morphological, and functional studies have been unable to parse interneurons into more than one or two subtypes (Charalambakis et al., 2019; Leist et al., 2016), making it difficult to study the specificity for loss of $Gad1^{+}$ cells in this retinorecipient brain region. In contrast, vLGN contains numerous transcriptionally distinct GABAergic cell types (including both local interneurons and projection neurons), some of which exhibit regional preferences, unique morphologies, and distinct connectivity (Fratzl et al., 2021; Sabbagh et al., 2021; Salay and Huberman, 2021). Thus, RGC-derived SHH may affect specific subtypes of GABAergic cells in vLGN. Unfortunately, we currently lack transcriptional or neurochemical markers to specifically label interneurons in vLGN (versus GABAergic projection neurons) making this challenging to address at this time.

It is also noteworthy that we observed more dramatic decrease in $Gad1^{+}$ cells in $Shh^{fl/fl};Nes^{Cre}$ mutants, particularly in the vLGN, compared to the reduction observed in either $Shh^{fl/fl};Calb2^{Cre}$ or $Atoh7^{-/-}$ mice. We interpret this to indicate multiple roles and sources of SHH contribute to thalamic development. In $Shh^{fl/fl};Nes^{Cre}$ mutants, SHH loss occurs much earlier in development and in progenitor zones (Lendahl et al., 1990; Zimmerman et al., 1994), likely impacting the generation of GABAergic progenitors that will eventually migrate into visual thalamus. Indeed, *Shh* null mice show defects in ventral patterning and a noticeable decrease in the size of their brain (Chiang et al., 1996; Machold et al., 2003; Rallu et al., 2002), indicating key roles for this morphogen in many aspects of early brain development. In $Shh^{fl/fl};Calb2^{Cre}$ mice, SHH is not deleted from many cells in these progenitor zones, suggesting to us that these results differentiate between progenitor zone-derived SHH functions and RGC-derived SHH functions. An alternative possibility, however, is that SHH is also generated by cells within visual thalamus, which could also potentially influence interneuron migration process. While we detect no to very low expression of *Shh* in neonatal visual thalamus with microarray and sequencing techniques, this could reflect technical limitation in these approaches or analysis at the wrong ages (Monavarfeshani et al., 2018; Su et al., 2011).

SHH signaling in RGC subtypes

Even though most RGC subtypes produce SHH, one fascinating question is whether there are any functional differences between those that express high versus low levels of this molecule. Clusters 16, 19, and 32 were notable for showing high SHH expression (Figure 3c). The transcription factor *Pou6f2* reported to specify these RGC types (Rheaume et al., 2018) is expressed in a novel class of On-OFF direction selective RGCs (DSGCs) (Li et al., 2020).

Conversely, RGC clusters 30 and 40 that are defined by transcription factor *Satb2* (Rheaume et al., 2018) showed very low or no expression of SHH (Figure 3c). *Satb2* is a selective marker for On–Off DSGCs encoding either posterior or anterior motion (Dhande et al., 2019). Why do DSGCs subtypes exhibit varying degrees of SHH expression? One possibility is that each DSGC subtypes contributes differently to interneuron development, some of which are independent of SHH. Indeed, retinal inputs are not only important for interneuron migration but also their absence leads to arrested arbor branching and dystrophic arbor field growth of these GABAergic cells (Charalambakis et al., 2019). Studies examining interneuron development under specific RGC subtype manipulation may provide further insight into these differences.

SHH signaling in astrocytes

While SHH signaling is well-characterized for its dynamic roles in neural precursor cells and oligodendrocytes (Belgacem et al., 2016), much less is known about its function in astrocyte development, particularly in the context of the developing visual system. In the optic nerve, SHH has been reported to be necessary for maintenance of astrocyte proliferation (Dakubo et al., 2008; Wallace and Raff, 1999). Our work demonstrates that this signaling pathway is also critical for the expression of *Fgf15* by thalamic astrocytes. However, only a small fraction of astrocytes express *Fgf15* in visual thalamus (Su et al., 2020), raising the questions of whether only some thalamic astrocytes generate the machinery to respond to SHH or whether retina-derived SHH itself can alter the identity of thalamic astrocytes to generate heterogeneity in these cells. In support of the latter possibility, neuron-derived SHH is integral for maintaining the identity of Bergmann glial cells, a specialized astrocyte type in the cerebellum (Farmer et al., 2016). However, it is important to note that we found that a much greater proportion of astrocytes in visual thalamus generate SHH signaling components, *Ptch1* and *Smo*, compared to those that generate *Fgf15*. One possibility is that all thalamic astrocytes can generate SHH-induced *Fgf15,* but they do it asynchronously. The widespread expression of SHH signaling components in thalamic astrocytes also suggests that this pathway could be important in ways beyond interneuron migration. Outside of the thalamus, SHH appears to be important for a variety of astrocytic functions, including modulation of neuronal activity (Hill et al., 2019) , regulation of energy metabolism (Tirou et al., 2021), and neuroprotection (Ugbode et al., 2017). These studies highlight the need to further explore the roles for SHH signaling in thalamic circuits.

Neuronal activity from RGCs and thalamic interneuron migration

Many developmental aspects underlying orderly connections in the mammalian visual system are dependent on retinal activity even before eye opening (D'Souza and Lang, 2020; Huberman et al., 2008). In the case of thalamic interneurons, the role of retinal activity in their migration, differentiation, or incorporation into thalamic circuits was unresolved prior to these studies. Application of tetrodotoxin in neonatal organotypic thalamic slices led to the suggestion that activity was necessary for directing the spatial incorporation of these interneurons into dLGN circuits (Golding et al., 2014). In the present study, we investigated whether *in vivo* RGC activity contributes to the initial recruitment of GABAergic interneurons into dLGN and vLGN. Our results revealed that decreasing retinal activity had little effect on the percentage of interneurons recruited into dLGN and vLGN. Although this genetic approach to inhibit neuronal activity has been shown to be effective in the developing hippocampus (Sando et al., 2017), it is possible that we may not have completely blocked the release of neurotransmitters from RGCs in *Rosa26*$^{floxstop\text{-}TeNT}$*;Calb2*^{Cre} mutants (because of incomplete expression of TeNT by all RGCs, developmentally regulated expression of TeNT or other confounding issues) and that the remaining activity was sufficient to directly influence the interneuron migration process. In fact, it is possible that retinal activity may even induce RGCs to release SHH. Although such roles of neuronal stimulation on SHH release have not been reported in visual thalamus, activity in hippocampal neurons has been shown to cause the release of SHH in a SNAREs- and Ca^{2+}- dependent manner (Su et al., 2017). We argue that is not the case based on the early and broad expression of Cre in the driver line applied here – ensuring all subtypes of RGCs will express TeNT at birth. Moreover, the impaired refinement of eye-specific RGC projections in *Rosa26*$^{floxstop\text{-}TeNT}$*;Calb2*^{Cre} mice similar to impairments induced by manipulation and blocking of retinal activity early in perinatal development (Huberman et al., 2003; Pfeiffenberger et al., 2005) suggests that activity is functionally reduced in these mutants. Overall, this suggests that retinal inputs have both activity-dependent and activity-independent roles in orchestrating the development of visual thalamus. The techniques typically used to study how retinal inputs impact the thalamic development, surgical or genetic removal of RGC axons from thalamus have failed to distinguish between these independent roles previously.

MATERIALS AND METHODS

Key resources table

Reagent type (species) or resource	Designation	Source or reference	Identifiers	Additional information
Antibody	anti-GFP (rabbit polyclonal)	Thermo Fisher Scientific	Cat#A-11122; RRID:AB_221569	1:250
Antibody	anti-S100 (rabbit polyclonal)	Dako	Cat# Z0311; RRID:AB_10013383	1:200
Antibody	anti-Calretinin (rabbit polyclonal)	Swant	Cat#7697; RRID: AB_2619710	1:1000
Antibody	anti-RFP (rabbit polyclonal)	Thermo Fisher Scientific	Cat#600-401-379-RTU; RRID:AB_2209751	1:500
Antibody	Anti-Digoxigenin-POD (sheep polyclonal)	Millipore Sigma	Cat#11207733910; RRID:AB_514500	1:1000
Antibody	Anti-Fluorescein-POD (sheep polyclonal)	Millipore Sigma	Cat#11426346910; RRID:AB_840257	1:1000
Biologic sample (Mus musculus)	*Rosa26*^{tdT}*;Gli1*^{CreER} brains	A.D.R Garcia, Drexel University	JAX #007913, #007914; RRID: IMSR_JAX:007913, IMSR_JAX:007914	
Peptide, recombinant protein	Fluorescein RNA Labeling Mix	Roche	Cat#11685619910	
Peptide, recombinant protein	DIG RNA Labeling Mix	Roche	Cat#11277073910	
Peptide, recombinant protein	SuperScript™ II Reverse Transcriptase	Thermo Fisher Scientific	Cat#18064022	
Peptide, recombinant protein	Cholera Toxin Subunit B (CTB, Recombinant), Alexa Fluor™ 488 Conjugate	Thermo Fisher Scientific	CAT#C22841	
Peptide, recombinant protein	Tamoxifen	Sigma	CAT#T5648-1G	
Peptide, recombinant protein	CTB (Recombinant), Alexa Fluor™ 555 Conjugate	Thermo Fisher Scientific	CAT#C34776	
Commercial assay, kit	SuperScript II Reverse Transcriptase First Strand cDNA Synthesis kit	Invitrogen	Cat#18064014	
Commercial assay, kit	pGEM-T Easy Vector Systems	Promega	Cat#A1360	
Commercial assay, kit	MAXIscript in vitro Transcription Kit	Ambion	Cat#AM1312	

Commercial assay, kit	Tyramide Signal Amplification system	PerkinElmer	Cat#NEL753001 KT	
Commercial assay, kit	iTaq™ Universal SYBR® Green Supermix	Bio-Rad	Cat#1725124	
Commercial assay, kit	Bio-Rad Total RNA Extraction from Fibrous and Fatty Tissue kit	Bio-Rad	Cat#7326870	
Commercial assay, kit	RNAscope® Multiplex Fluorescent Reagent Kit V2	Advanced Cell Diagnostics (ACD)	Cat#323100	
Other	RNAseq datasets for the developing mouse dLGN and vLGN	DOI: https://doi.org/10.7554/eLife.33498.006		Monavarfeshani et al., 2018
Other	single-cell RNAseq dataset for RGC subtypes	DOI: https://doi.org/10.1038/s41467-018-05134-3	Accession # GSE115404	Rheaume et al., 2018
Other	single-cell RNAseq dataset for RGCs at various ages	DOI: https://doi.org/10.7554/eLife.73809	Accession # GSE185671	Shekhar et al., 2022
Strain, strain background (*Mus musculus*)	C57BL/6J mice	The Jackson Laboratory	JAX#000664; RRID:IMSR_JAX:000664	
Strain, strain background (*Mus musculus*)	*Calb2*^{Cre}	The Jackson Laboratory	JAX#010774; RRID:IMSR_JAX:010774	
Strain, strain background (*Mus musculus*)	*Shh*$^{fl/fl}$	The Jackson Laboratory	JAX#004293; RRID:IMSR_JAX:004293	
Strain, strain background (*Mus musculus*)	*Nes*^{Cre}	The Jackson Laboratory	JAX#003771; RRID:IMSR_JAX:003771	
Strain, strain background (*Mus musculus*)	*Aldh1l1-GFP*	S. Robel, Virginia Tech	Stock#011015-UCD; RRID: MMRRC_011015-UCD	
Strain, strain background (*Mus musculus*)	*Rosa26*$^{floxstop\text{-}TeNT}$	A. Maximov, The Scripps Research Institute	MGI:3839913	Zhang et al., 2008
Strain, strain background (*Mus musculus*)	*Rosa26*^{tdT}(Ai14)	The Jackson Laboratory	JAX#007914; RRID: IMSR_JAX:007914	
Strain, strain background (*Mus musculus*)	*Gli1*^{CreER}	Ahn and Joyner, 2005	JAX#007913; RRID: IMSR_JAX:007913	
Strain, strain background (*Mus musculus*)	*Rosa26*^{tdT}	The Jackson Laboratory	JAX#007909; RRID:IMSR_JAX:007909	
Strain, strain background (*Mus musculus*)	*Atoh7*$^{-/-}$	S. W. Wang, University of	Stock# 042298-UCD;	

		Texas MD Anderson Cancer Center	RRID:MMRRC_042298-UCD	
Strain, strain background (*Mus musculus*)	*Gli1*$^{nlacZ/+}$	The Jackson Laboratory	JAX#008211; RRID:IMSR_JAX:008211	Bai et al., 2022
Sequence-base reagent	Gad1 cloning primer F:TGTGCCCAAACTGGTCCT; R:TGGCCGATGATTCTGGTT	Integrated DNA Technologies	N/A	
Sequence-base reagent	Gja1 cloning primer F:CGTGAAGGGAAGAAGCGA; R:GCCTGCAAACTGCCAAGT	Integrated DNA Technologies	N/A	
Sequence-base reagent	Shh qPCR primer F:ACGTAGCCGAGAAGACCCTA; R:ACTTGTCTTTGCACCTCTGAGT	Integrated DNA Technologies	N/A	
Sequence-base reagent	Gapdh qPCR primer F:CGTCCCGTAGACAAAATGGT; R:TTGATGGCAACAATCTCCAC	Integrated DNA Technologies	N/A	
Sequence-base reagent	18s qPCR primer F:GGACCAGAGCGAAAGCATTTG; R:GCCAGTCGGCATCGTTTATG	Integrated DNA Technologies	N/A	
Sequence-base reagent	Cre genotyping primer F:CGTACTGACGGTGGGAGAAT; R:TGCATGATCTCCGGTATTGA	Integrated DNA Technologies	N/A	
Sequence-base reagent	*Shh*$^{fl/fl}$ genotyping primer F:CAGAGAGCATTGTGGAATGG R:CAGACCCTTCTGCTCATGG	Integrated DNA Technologies	N/A	
Sequence-base reagent	tdT genotyping primer F: ACCTGGTGGAGTTCAAGACCATCT; R:TTGATGACGGCCATGTTGTTGTCC	Integrated DNA Technologies	N/A	
Sequence-base reagent	GFP genotyping primer F:AAGTTCATCTGCACCACCG; R:TCCTTGAAGAAGATGGTGCG	Integrated DNA Technologies	N/A	
Sequence-base reagent	TeNT genotyping primer FA:AAAGTCGCTCTGAGTTGTTAT;	Integrated DNA Technologies	N/A	

	RA:GGAGCGGGAG AAATGGATATG; SA:CATCAAGGAAA CCCTGGACTACTG			
Sequence-base reagent	*Atoh7*$^{-/-}$ genotyping primer (to see the wild type band) F:ATGGCGCTCAG CTACATCAT; R:GGGTCTACCTG GAGCCTAGC	Integrated DNA Technologies	N/A	
Sequence-base reagent	*Neo* genotyping primer (to see the mutant *Atoh7* band) F:GCCGGCCACAG TCGATGAATC R:CATTGAACAAGA TGGATTGCA	Integrated DNA Technologies	N/A	
Recombinant DNA reagent	Mouse Fgf15 cDNA	Horizon (Dharmacon)	Cat#MMM1013-202768318, Clone ID: 5066286	
Recombinant DNA reagent	RNA scope probe-Mm-Smo	ACD	Cat#318411	
Recombinant DNA reagent	RNA scope probe-Mm-Ptch1-C2	ACD	Cat#402811-C2	
Recombinant DNA reagent	RNA scope probe-Mm-Shh-C3	ACD	Cat#314361-C3	
Recombinant DNA reagent	RNA scope 3-plex positive control probe-mm	ACD	Cat#320881	
Recombinant DNA reagent	RNA scope 3-plex negative control probe-mm	ACD	Cat#320871	
Software, algorithm	Prism	GraphPad	version 8.0.; RRID: SCR_002798	
Software, algorithm	Adobe Photoshop	Adobe Inc.	version: 21.1.2	
Software, algorithm	ZEN black edition	Carl Zeiss	version: 14.0.12.201	
Software, algorithm	Fiji ImageJ	NIH	version: 1.52p	
Software, algorithm	RStudio	RStudio, Inc.	version: 1.2.5042	
Other	*Fgf15* riboprobe	This paper	N/A	Information in “Riboprobe production”
Other	*Gad1* riboprobe	This paper	N/A	Information in “Riboprobe production”
Other	*Gja1* riboprobe	This paper	N/A	Information in “Riboprobe production”

Animals

C57BL/6J, *Calb2*^{Cre}, *Shh*$^{fl/fl}$, *Nes*^{Cre} , and *Rosa26*^{tdT} mice were obtained from The Jackson Laboratory. *Atoh7*$^{-/-}$ mice were obtained from S. W. Wang (University of Texas MD Anderson Cancer Center, Houston, TX). *Aldh1l1-GFP* mice were provided by S. Robel (Virginia Tech, Roanoke, VA). *Rosa26*$^{floxstop\text{-}TeNT}$ mice were obtained from A. Maximov (The Scripps Research Institute, La Jolla, CA), after receiving approval from M. Goulding (The Salk Institute for Biological Studies, La Jolla, CA). Tissue from *Gli1*$^{nlacZ/+}$ mice was obtained from A. D. R. Garcia (Drexel University, Philadelphia, PA). We were unable to breed *Rosa26*$^{floxstop\text{-}TeNT}$*;Calb2*^{Cre} with homozygous TeNT, possibly due to embryonic death. Thus, for any activity-related experiment presented in Figure 1 and Figure 1—figure supplement 2, mice heterozygous for the TeNT allele were considered as mutant mice. The key resources table includes sequences for the genotyping primers. *Gli1*^{CreER} mice (Ahn and Joyner, 2005) were crossed with Ai14 reporter mice (JAX #007914) to generate *Rosa26*^{tdT}*;Gli1*^{CreER} mice.

Ethics

Both sexes were used for all experiments. Animals had *ad libitum* access to water and food and were housed in a temperature-controlled environment and in a 12-hour light/dark cycle. The experiments were approved by the Virginia Tech Institutional Animal Care and Use Committee.

Preparation of tissue and IHC

As previously described, tribromoethanol (Avertin) was intraperitoneally injected into mice at a concentration of 12.5 µg/ml. The animals were trans-cardially perfused with PBS and 4% paraformaldehyde (PFA, pH 7.4) (Su et al., 2010). Brains were kept overnight at 4°C in 4% PFA, and then transferred to 30% sucrose in PBS for at least 48 hours. The fixed brains were embedded in Tissue Freezing Medium (Electron Microscopy Sciences) and 16 µm thick sections were cryosectioned on a Leica CM1850 cryostat. Following air-drying for 30 minutes, slides were incubated in IHC blocking buffer (2.5% bovine serum albumin, 5% normal goat serum, 0.1% Triton-X in PBS) for 30 minutes. Primary antibodies were diluted in blocking buffer and incubated on the sections at 4°C for >18 hours (information on the antibodies is available in the key resources table). Following washing with PBS, fluorophore-conjugated secondary antibodies (Invitrogen) were incubated on tissue sections for 1 hour at room temperature. The sections were stained with 4′,6-diamidino-2-phenylindole (DAPI) after several washes in PBS and mounted with Vectashield (Vector Laboratories). Brightfield βGal staining was performed as previously described staining (Garcia et al., 2010).

Riboprobe production

Riboprobes were generated as described previously (Monavarfeshani et al., 2018; Su et al., 2010). Plasmids carrying *Fgf15* were purchased from GE Dharmacon. *Gad1* 1 Kb cDNA (corresponding to nucleotides 1099–2081) and *Gja1* 1.1 Kb cDNA (corresponding to nucleotides 714–1854) were generated using SuperScript II Reverse Transcriptase First Strand cDNA Synthesis kit and the manufacturer's protocol. The information for the sequence of cloning primers is in the key resources table. cDNA was then cloned into the pGEM-T Easy vector. We generated sense and antisense riboprobes against *Fgf15*, *Gad1*, and *Gja1* from linearized plasmids using DIG- or FL-labeled uridylyltransferase and MAXIscript in vitro Transcription Kit. Riboprobes were hydrolyzed into ~500 bp fragments by adding 6 µl of Na_2CO_3 (1 M), 4 µl of $NaHCO_3$ (1 M), and 80 µl of water at 60°C. Following precipitation with ethanol, the riboprobes were dissolved in RNAase-free water.

Tamoxifen administration

Tamoxifen was dissolved in corn oil at 5 mg/ml. Tamoxifen was administered by intragastric injection to *Rosa26*^{tdT}*;Gli1*^{CreER} pups at P0.

In situ hybridization (ISH) with in-house generated riboprobes

We performed ISH using the generated riboprobes on PFA-fixed, cryosectioned 16 µm tissue as described previously (Monavarfeshani et al., 2018). The sections were fixed in 4% PFA for 10 minutes, washed with PBS, and incubated with proteinase K (1 µg/mL in 50 mM Tris pH 7.5, 5 mM EDTA) solution for 10 minutes. After being washed with PBS, sections were incubated for 5 minutes in 4% PFA, washed with PBS, and then incubated for 10 minutes in acetylation solution (0.25% acetic anhydride, 20 mM hydrochloric acid and 1.33% triethanolamine). In order to permeabilize them, sections were incubated for 30 minutes in 1% triton in PBS. For blocking endogenous peroxidase, sections were incubated in 0.3% hydrogen peroxide in PBS for 30 minutes, then rinsed in PBS. We equilibrated the sections in hybridization solution (50

mL of prehyb solution, 1.6 ml of 5 mg/ml, and 25 mg Roche yeast RNA) for 1 hour, and then incubated them in heat-denatured diluted riboprobes (10 minutes at 80°C) overnight at 65°C. On the next day, slides were rinsed with 0.2x saline-sodium citrate solution followed by tris-buffered saline (TBS). Following 1 hour incubation in blocking buffer (10% lamb serum, 0.2% Roche blocking reagent in TBS), the slides were incubated overnight at 4◦C in HRP-conjugated anti-DIG or anti-FL antibodies. On day three, riboprobes were identified using a Tyramide Signal Amplification (TSA) system.

ISH with commercially generated RNAscope riboprobes

The probes used were RNA scope probe-Mm-Smo, RNA scope probe-Mm-Ptch1-C2, RNA scope probe-Mm-Shh-C3, RNA scope 3-plex positive control probe-mm, and RNA scope 3-plex negative control probe-mm. PFA-fixed, cryosectioned 16 µm tissue were processed for RNA Scope Multiplex using manufacturer's protocol. Briefly, sections were dehydrated by ethanol treatment and then pretreated with target retrieval reagent and protease III. Following the hybridization of probes, we amplified signals on sections using the TSA system.

Intraocular injection of CTB

We anesthetized mice with isoflurane or hypothermia for intraocular injections, as described previously (Jaubert-Miazza et al., 2005). A fine glass pipette attached to a picospritzer was used to inject 1–2 µl of CTB, 1 mg/ml, intravitreally into the eye. After 2-3 days, mice were perfused, and their PFA-fixed brains were sectioned (100 µm) using a Vibratome (HM650v, Thermo Fisher Scientific) and mounted with Vectashield.

Imaging

A Zeiss LSM700 confocal microscope was used for image acquisition. Each representative image in the figure is a maximum intensity projection. Colocalization was confirmed using single-plane images.

qRT-PCR

RNA was isolated from non-pooled P3 control and *Shh*$^{fl/fl}$*;Calb2*^{Cre} mutant retina using the Bio-Rad Total RNA Extraction from Fibrous and Fatty Tissue kit and manufacturer's protocol. Using this RNA, cDNAs were generared with SuperScript™ II Reverse Transcriptase. qPCR was performed using iTaq™ Universal SYBR® Green Supermix on a CFX Connect Real-Time system (BioRad). Cyling conditions for 500 or 1000 ng of cDNA are as follows: 95°C for 30 seconds and 42 cycles of amplification (95°C for 10 seconds, 60°C for 30 seconds) followed by a melting curve analysis. Each individual run included separate 18S rRNA or glyceraldehyde-3-phosphate dehydrogenase (*gapdh*) control reactions. Using the $2^{-\Delta\Delta CT}$ method, we determined the relative quantities of RNA (Schmittgen and Livak, 2008). The primer list can be found in the key resources table.

Looming visual stimulus assay

The looming visual stimulus assay was performed as described previously (Su et al., 2021). Mice were presented with an overhead looming stimulus in a white rectangular arena (47 × 37 × 30 cm). To maintain uniform environmental conditions, the arena was illuminated evenly from above and enclosed in a light-proof, sound-isolating room. One of the corners had an opaque shelter, whose entrance faced the center of the arena. On the stand next to the arena, a camera was mounted to capture mouse behavior. The mice were only tested once each to prevent habituation to the stimulus. Ten minutes prior to the recording of the test, the animals were free to explore the arena and the shelter. Looming stimulus began when the animal moved around the center of the arena. Ten seconds of video was recorded prior to, during, and after the stimulus onset. We manually scored the animal's behavior during 10 seconds of looming stimulus. The reaction time was defined as a period of one or more seconds in which the animal either freezes, runs, or hides in the shelter after the stimulus began.

QUANTIFICATION AND STATISTICAL ANALYSIS

A minimum of three biological replicates per genotype and age and a minimum of three dLGN/vLGN sections per animal were used for all quantification, based on observed variability and prior experience (Sabbagh et al., 2018, 2021; Su et al., 2020). We did not exclude any data or animals from our analyses. No sex-specific differences were observed. Statistical analyses (Student's *t*-test) were performed using GraphPad Prism (version 8.0). $P < 0.05$ values were considered to be significantly different. The figure legends provide *P* values for all experiments. Data are plotted as mean ± SEM.

Percentage of *Gad1*$^+$, *Gja1*$^+$ and *Gli1-tdT*$^+$ cells

Images were obtained using 10x magnification. We quantified *Gad1*$^+$, *Gja1*$^+$ (by ISH) and *Gli1-tdT*$^+$ (by *Rosa26*^{tdT};*Gli1*^{CreER} reporter mice) cells and divided by DAPI$^+$ cells counted in that tissue section. “Count Tool” function in Adobe Photoshop (version: 21.1.2) was utilized for counting purposes.

Density of *Fgf15*$^+$ cells

Images were obtained using 10x magnification. We quantified *Fgf15*$^+$ (by ISH) cells and normalized them to the area of dLGN or vLGN. Areas were measured by outlining the boundaries of dLGN or vLGN using ZEN 2.3 SP1 FP1 (black) edition (version: 14.0.12.201, Carl Zeiss).

CTB analysis

Images were obtained using 10x magnification and Fiji ImageJ (version: 1.52p, NIH) was used for analyses. Using “Split Channels”, CTB 488 and CTB 555 signal were separated. For each channel, contrast was enhanced (“Enhance Contrast”, 0.3%), background was subtracted (“Subtract Background”, 1000 pixels and “Math”, “Subtract”), and channels were binarized (“Make Binary”). The dLGN boundary was drawn manually by utilizing the “Freehand selections” tool. Using this boundary and “Area fraction” on each binarized channel, percentage of dLGN covered by ipsiRGCs or contraRGCs was determined. To obtain the overlap channel, we used “AND” function in “Image Calculator”. On this channel, the dLGN boundary was drawn and “Area fraction” gave the percentage of dLGN area covered by the overlap of ipsi and contraRGCs projections.

RNAscope analysis

Images were acquired at 20x magnification. We used ACD’s scoring criteria for this analysis (https://acdbio.com/dataanalysisguide). A cell was classified as positive for *Ptch1* or *Smo* (by RNAscope) if it contained at least 10 dots. This was divided by *Aldh1l1-GFP*$^+$ cells (by *Aldh1l1-GFP* transgenic line) to obtain percentage of astrocytes that express *Ptch1* or *Smo* in dLGN and vLGN. “Count Tool” function in Adobe Photoshop was utilized for counting purposes.

Calb2 and *Shh* expression in RGC clusters

Single cell data from Rheaume et al., 2018 was downloaded from NCBI GEO (accession #: GSE115404). *Shh* (Ensembl ID = ENSMUSG00000002633) and *Calb2* (Ensemble ID = ENSMUSG00000003657) expression values were used to generate “ggplot2” on RStudio (version: 1.2.5042, RStudio, Inc.).

Data availability

This paper analyzes three existing and publicly available data: 1) Data from Monavarfeshani et al., 2018 can be found at https://elifesciences.org/articles/33498. The DOI is listed in the key resources table, 2) Data from Rheaume et al., 2018 can be found at https://health.uconn.edu/neuroregeneration-lab/rgc-subtypes-gene-browser/. 3) Data from Shekhar et al., 2022 can be found at https://elifesciences.org/articles/73809. The accession number and DOI are listed in the key resources table.

REFERENCES

Ahmadlou, M., Zweifel, L.S., and Heimel, J.A. (2018). Functional modulation of primary visual cortex by the superior colliculus in the mouse. Nat. Commun. *9*, 3895.

Ahn, S., and Joyner, A.L. (2005). In vivo analysis of quiescent adult neural stem cells responding to Sonic hedgehog. Nature *437*, 894–897.

Arcelli, P., Frassoni, C., Regondi, M.C., Biasi, S. De, and Spreafico, R. (1997). GABAergic neurons in mammalian thalamus: A marker of thalamic complexity? Brain Res. Bull. *42*, 27–37.

Belgacem, Y.H., Hamilton, A.M., Shim, S., Spencer, K.A., and Borodinsky, L.N. (2016). The Many Hats of Sonic Hedgehog Signaling in Nervous System Development and Disease. J. Dev. Biol. *4*.

Bickford, M.E., Slusarczyk, A., Dilger, E.K., Krahe, T.E., Kucuk, C., and Guido, W. (2010). Synaptic development of the mouse dorsal lateral geniculate nucleus. J. Comp. Neurol. *518*, 622–635.

Brooks, J.M., Su, J., Levy, C., Wang, J.S., Seabrook, T.A., Guido, W., and Fox, M.A. (2013). A molecular mechanism regulating the timing of corticogeniculate innervation. Cell Rep. *5*, 573–581.

C. Brunjes, P. (1994). Unilateral naris closure and olfactory system development. Brain Res. Rev. *19*, 146–160.

Charalambakis, N.E., Govindaiah, G., Campbell, P.W., and Guido, W. (2019). Developmental remodeling of thalamic interneurons requires retinal signaling. J. Neurosci. *39*, 3856–3866.

Chiang, C., Litingtung, Y., Lee, E., Young, K.E., Corden, J.L., Westphal, H., and Beachy, P.A. (1996). Cyclopia and defective axial patterning in mice lacking Sonic hedgehog gene function. Nature *383*, 407–413.

Ciftcioglu, U.M., Suresh, V., Ding, K.R., Sommer, F.T., and Hirsch, J.A. (2020). Visual Information Processing in the Ventral Division of the Mouse Lateral Geniculate Nucleus of the Thalamus. J. Neurosci. *40*, 5019–5032.

Crombie, D., and Busse, L. (2021). Should I stay or should I go? A thalamic circuit for modulating behavioral responses to visual threat. Neuron *109*, 3717–3719.

D'Souza, S., and Lang, R.A. (2020). Retinal ganglion cell interactions shape the developing mammalian visual system. Development *147*, 1–13.

Dakubo, G.D., Beug, S.T., Mazerolle, C.J., Thurig, S., Wang, Y., and Wallace, V.A. (2008). Control of glial precursor cell development in the mouse optic nerve by sonic hedgehog from retinal ganglion cells. Brain Res. *1228*, 27–42.

Dhande, O.S., Stafford, B.K., Franke, K., El-Danaf, R., Percival, K.A., Phan, A.H., Li, P., Hansen, B.J., Nguyen, P.L., Berens, P., et al. (2019). Molecular fingerprinting of on–off direction-selective retinal ganglion cells across species and relevance to primate visual circuits. J. Neurosci. *39*, 78–95.

Evangelio, M., García-Amado, M., and Clascá, F. (2018). Thalamocortical projection neuron and interneuron numbers in the visual thalamic nuclei of the adult C57BL/6 mouse. Front. Neuroanat. *12*, 1–12.

Farmer, W.T., Abrahamsson, T., Chierzi, S., Lui, C., Zaelzer, C., Jones, E. V., Bally, B.P., Chen, G.G., Théroux, J.F., Peng, J., et al. (2016). Neurons diversify astrocytes in the adult brain through sonic hedgehog signaling. Science (80-.). *351*, 849–854.

Fratzl, A., Koltchev, A.M., Vissers, N., Tan, Y.L., Marques-Smith, A., Stempel, A.V., Branco, T., and Hofer, S.B. (2021). Flexible inhibitory control of visually evoked defensive behavior by the ventral lateral geniculate nucleus. Neuron *109*, 3810-3822.e9.

Garcia, A.D.R., Petrova, R., Eng, L., and Joyner, A.L. (2010). Sonic Hedgehog regulates discrete populations of astrocytes in the adult mouse forebrain. J. Neurosci. *30*, 13597–13608.

Garcia, A.D.R., Han, Y.G., Triplett, J.W., Farmer, W.T., Harwell, C.C., and Ihrie, R.A. (2018). The elegance of sonic hedgehog: Emerging novel functions for a classic morphogen. J. Neurosci. *38*, 9338–9345.

Golding, B., Pouchelon, G., Bellone, C., Murthy, S., Di Nardo, A.A., Govindan, S., Ogawa, M., Shimogori, T., Lüscher, C., Dayer, A., et al. (2014). Retinal input directs the recruitment of inhibitory interneurons into thalamic visual circuits. Neuron *81*, 1057–1069.

Grant, E., Hoerder-Suabedissen, A., and Molnar, Z. (2016). The Regulation of Corticofugal Fiber Targeting by Retinal Inputs. Cereb. Cortex *26*, 1336–1348.

Guido, W. (2018). Development, form, and function of the mouse visual thalamus. J. Neurophysiol. *120*, 211–225.

Harrington, M.E. (1997). The VentralLateralGeniculateNucleusandthe Intergeniculate Leaflet:IntenelatedStructures in the Visual andCircadianSystems. Neurosci. AndBiobehavioral Rev. *21*, 705–727.

He, J., Xu, X., Monavarfeshani, A., Banerjee, S., Fox, M.A., and Xie, H. (2019). Retinal-input-induced epigenetic dynamics in the developing mouse dorsal lateral geniculate nucleus. Epigenetics and Chromatin *12*, 1–16.

Hill, S.A., Blaeser, A.S., Coley, A.A., Xie, Y., Shepard, K.A., Harwell, C.C., Gao, W.-J., and Garcia, A.D.R. (2019). Sonic hedgehog signaling in astrocytes mediates cell type-specific synaptic organization. Elife *8*, 1–23.

Van Horn, S.C., Erişir, A., and Sherman, S.M. (2000). Relative distribution of synapses in the A-laminae of the lateral geniculate nucleus of the cat. J. Comp. Neurol. *416*, 509.

Huang, L., Xi, Y., Peng, Y., Yang, Y., Huang, X., Fu, Y., Tao, Q., Xiao, J., Yuan, T., An, K., et al. (2019). A Visual Circuit Related to Habenula Underlies the Antidepressive Effects of Light Therapy. Neuron *102*, 128-142.e8.

Huberman, A.D., Wang, G.Y., Liets, L.C., Collins, O.A., Chapman, B., and Chalupa, L.M. (2003). Eye-specific retinogenicu late segregation independent of normal neuronal activity. Science (80-.). *300*, 994–998.

Huberman, A.D., Feller, M.B., and Chapman, B. (2008). Mechanisms underlying development of visual maps and receptive fields. Annu. Rev. Neurosci. *31*, 479–509.

Ihrie, R.A., Shah, J.K., Harwell, C.C., Levine, J.H., Guinto, C.D., Lezameta, M., Kriegstein, A.R., and Alvarez-Buylla, A. (2011). Persistent Sonic Hedgehog Signaling in Adult Brain Determines Neural Stem Cell Positional Identity. Neuron *71*, 250–262.

Ishibashi, M., and McMahon, A.P. (2002). A sonic hedgehog-dependent signaling relay regulates growth of diencephalic and mesencephalic primordia in the early mouse embryo. Development *129*, 4807–4819.

Jager, P., Ye, Z., Yu, X., Zagoraiou, L., Prekop, H.T., Partanen, J., Jessell, T.M., Wisden, W., Brickley, S.G., and Delogu, A. (2016). Tectal-derived interneurons contribute to phasic and tonic inhibition in the visual thalamus. Nat. Commun. *7*, 1–14.

Jager, P., Moore, G., Calpin, P., Durmishi, X., Salgarella, I., Menage, L., Kita, Y., Wang, Y., Kim, D.W., Blackshaw, S., et al. (2021). Dual midbrain and forebrain origins of thalamic inhibitory interneurons. Elife *10*, 1–29.

Jaubert-Miazza, L., Green, E., Lo, F.S., Bui, K., Mills, J., and Guido, W. (2005). Structural and functional composition of the developing retinogeniculate pathway in the mouse. Vis. Neurosci. *22*, 661–676.

Jensen, A.M., and Wallace, V.A. (1997). Expression of Sonic hedgehog and its putative role as a precursor cell mitogen in the developing mouse retina. Development *124*, 363–371.

Katz, L.C., and Shatz, C.J. (1996). Synaptic Activity and the Construction of Cortical Circuits. Science (80-.). *274*, 1133–1138.

Kerr, A., Patel, P.A., LaConte, L.E.W., Liang, C., Chen, C.K., Shah, V., Fox, M.A., and Mukherjee, K. (2019). Non-Cell Autonomous Roles for CASK in Optic Nerve Hypoplasia. Invest. Ophthalmol. Vis. Sci. *60*, 3584–3594.

Kim, J.J., Jiwani, T., Erwood, S., Loree, J., and Rosenblum, N.D. (2018). Suppressor of fused controls cerebellar neuronal differentiation in a manner modulated by GLI3 repressor and Fgf15. Dev. Dyn. *247*, 156–169.

Koehler, C.C., Hall, L.M., Hellmer, C.B., and Ichinose, T. (2019). Using looming visual stimuli to evaluate mouse vision. J. Vis. Exp. *2019*, 100–106.

Komada, M., Saitsu, H., Kinboshi, M., Miura, T., Shiota, K., and Ishibashi, M. (2008a). Hedgehog signaling is involved in development of the neocortex. Development *135*, 2717–2727.

Komada, M., Saitsu, H., Shiota, K., and Ishibashi, M. (2008b). Expression of Fgf15 is regulated by both activator and repressor forms of Gli2 in vitro. Biochem. Biophys. Res. Commun. *369*, 350–356.

Krahe, T.E., El-Danaf, R.N., Dilger, E.K., Henderson, S.C., and Guido, W. (2011). Morphologically distinct classes of relay cells exhibit regional preferences in the dorsal lateral geniculate nucleus of the mouse. J. Neurosci. *31*, 17437–17448.

Land, P.W., Kyonka, E., and Shamalla-Hannah, L. (2004). Vesicular glutamate transporters in the lateral geniculate nucleus: expression of VGLUT2 by retinal terminals. Brain Res. *996*, 251–254.

Leist, M., Datunashvilli, M., Kanyshkova, T., Zobeiri, M., Aissaoui, A., Cerina, M., Romanelli, M.N., Pape, H.C., and Budde, T. (2016). Two types of interneurons in the mouse lateral geniculate nucleus are characterized by different h-current density. Sci. Rep. *6*, 1–15.

Lendahl, U., Zimmerman, L.B., and McKay, R.D.G. (1990). CNS stem cells express a new class of intermediate filament protein. Cell *60*, 585–595.

Li, Y., Wang, J., King, R., and Geisert, E.E. (2020). POU6F2 Positive Retinal Ganglion Cells a Novel Group of ON-OFF Directionally Selective Subtypes in the Mouse Retina. BioRxiv Genet.

Link, E., Edelmann, L., Chou, J.H., Binz, T., Yamasaki, S., Eisel, U., Baumert, M., Südhof, T.C., Niemann, H., and Jahn, R. (1992). Tetanus toxin action: Inhibition of neurotransmitter release linked to synaptobrevin proteolysis. Biochem. Biophys. Res. Commun. *189*, 1017–1023.

Lizen, B., Claus, M., Jeannotte, L., Rijli, F.M., and Gofflot, F. (2015). Perinatal induction of Cre recombination with tamoxifen. Transgenic Res. *24*, 1065–1077.

Machold, R., Hayashi, S., Rutlin, M., Muzumdar, M.D., Nery, S., Corbin, J.G., Gritli-Linde, A., Dellovade, T., Porter, J.A., Rubin, L.L., et al. (2003). Sonic hedgehog is required for progenitor cell maintenance in telencephalic stem cell niches. Neuron *39*, 937–950.

Marigo, V., Laufer, E., Nelson, C.E., Riddle, R.D., Johnson, R.L., and Tabin, C. (1996). Sonic hedgehog regulates patterning in early embryos. Biochem. Soc. Symp. *62*, 51—60.

Martinez-Ferre, A., Lloret-Quesada, C., Prakash, N., Wurst, W., Rubenstein, J.L.R., and Martinez, S. (2016). Fgf15 regulates thalamic development by controlling the expression of proneural genes. Brain Struct. Funct. *221*, 3095–3109.

Monavarfeshani, A., Sabbagh, U., and Fox, M.A. (2017). Not a one-trick pony: Diverse connectivity and functions of the rodent lateral geniculate complex. Vis. Neurosci. *34*, E012.

Monavarfeshani, A., Stanton, G., Van Name, J., Su, K., Mills, W.A., Swilling, K., Kerr, A., Huebschman, N.A., Su, J., and Fox, M.A. (2018). LRRTM1 underlies synaptic convergence in visual thalamus. Elife *7*, 1–24.

Nithianantharajah, J., and Hannan, A.J. (2006). Enriched environments, experience-dependent plasticity and disorders of the nervous system. Nat. Rev. Neurosci. *7*, 697–709.

Ornitz, D.M., and Itoh, N. (2015). The fibroblast growth factor signaling pathway. Wiley Interdiscip. Rev. Dev. Biol. *4*, 215–266.

Peng, J., Fabre, P.J., Dolique, T., Swikert, S.M., Kermasson, L., Shimogori, T., and Charron, F. (2018). Sonic Hedgehog Is a Remotely Produced Cue that Controls Axon Guidance Trans-axonally at a Midline Choice Point. Neuron *97*, 326-340.e4.

Penn, A.A., Riquelme, P.A., Feller, M.B., and Shatz, C.J. (1998). Competition in retinogeniculate patterning driven by spontaneous activity. Science (80-.). *279*, 2108–2112.

Pfeiffenberger, C., Cutforth, T., Woods, G., Yamada, J., Rentería, R.C., Copenhagen, D.R., Flanagan, J.G., and Feldheim, D.A. (2005). Ephrin-As and neural activity are required for eye-specific patterning during retinogeniculate mapping. Nat. Neurosci. *8*, 1022–1027.

Rallu, M., Machold, R., Gaiano, N., Corbin, J.G., McMahon, A.P., and Fishell, G. (2002). Dorsoventral patterning is established in the telencephalon of mutants lacking both Gli3 and hedgehog signaling. Development *129*, 4963–4974.

Rheaume, B.A., Jereen, A., Bolisetty, M., Sajid, M.S., Yang, Y., Renna, K., Sun, L., Robson, P., and Trakhtenberg, E.F. (2018). Single cell transcriptome profiling of retinal ganglion cells identifies cellular subtypes. Nat. Commun. *9*.

Sabbagh, U., Monavarfeshani, A., Su, K., Zabet-Moghadam, M., Cole, J., Carnival, E., Su, J., Mirzaei, M., Gupta, V., Salekdeh, G.H., et al. (2018). Distribution and development of molecularly distinct perineuronal nets in visual thalamus. J. Neurochem. *147*, 626–646.

Sabbagh, U., Govindaiah, G., Somaiya, R.D., Ha, R. V., Wei, J.C., Guido, W., and Fox, M.A. (2021). Diverse GABAergic neurons organize into subtype-specific sublaminae in the ventral lateral geniculate nucleus. J. Neurochem. *159*, 479–497.

Saitsu, H., Komada, M., Suzuki, M., Nakayama, R., Motoyama, J., Shiota, K., and Ishibashi, M. (2005). Expression of the mouse Fgf15 gene is directly initiated by Sonic hedgehog signaling in the diencephalon and midbrain. Dev. Dyn. *232*, 282–292.

Salay, L.D., and Huberman, A.D. (2021). Divergent outputs of the ventral lateral geniculate nucleus mediate visually evoked defensive behaviors. Cell Rep. *37*, 109792.

Sando, R., Bushong, E., Zhu, Y., Huang, M., Considine, C., Phan, S., Ju, S., Uytiepo, M., Ellisman, M., and Maximov, A. (2017). Assembly of Excitatory Synapses in the Absence of Glutamatergic Neurotransmission. Neuron *94*, 312-321.e3.

Sanes, J.R., and Lichtman, J.W. (2001). Induction, assembly, maturation and maintenance of a postsynaptic apparatus. Nat. Rev. Neurosci. *2*, 791–805.

Schmittgen, T.D., and Livak, K.J. (2008). Analyzing real-time PCR data by the comparative CT method. Nat. Protoc. *3*, 1101–1108.

Schoch, S., Deák, F., Königstorfer, A., Mozhayeva, M., Sara, Y., Südhof, T.C., and Kavalali, E.T. (2001). SNARE function analyzed in synaptobrevin/VAMP knockout mice. Science (80-.). *294*, 1117–1122.

Seabrook, T.A., El-Danaf, R.N., Krahe, T.E., Fox, M.A., and Guido, W. (2013). Retinal input regulates the timing of corticogeniculate innervation. J. Neurosci. *33*, 10085–10097.

Shekhar, K., Whitney, I.E., Butrus, S., Peng, Y.R., and Sanes, J.R. (2022). Diversification of multipotential postmitotic mouse retinal ganglion cell precursors into discrete types. Elife *11*.

Sherman, S.M., and Guillery, R.W. (2002). The role of the thalamus in the flow of information to the cortex. Philos. Trans. R. Soc. B Biol. Sci. *357*, 1695–1708.

Somaiya, R.D., Huebschman, N.A., Chaunsali, L., Sabbagh, U., Carrillo, G.L., Tewari, B.P., and Fox, M.A. (2021). Development of astrocyte morphology and function in mouse visual thalamus. J. Comp. Neurol. 1–18.

Su, J., Gorse, K., Ramirez, F., and Fox, M.A. (2010). Collagen XIX is expressed by interneurons and contributes to the formation of hippocampal synapses. J. Comp. Neurol. *518*, 229–253.

Su, J., Haner, C. V., Imbery, T.E., Brooks, J.M., Morhardt, D.R., Gorse, K., Guido, W., and Fox, M.A. (2011). Reelin is required for class-specific retinogeniculate targeting. J. Neurosci. *31*, 575–586.

Su, J., Charalambakis, N.E., Sabbagh, U., Somaiya, R.D., Monavarfeshani, A., Guido, W., and Fox, M.A. (2020). Retinal inputs signal astrocytes to recruit interneurons into visual thalamus. Proc. Natl. Acad. Sci. U. S. A. *117*, 2671–2682.

Su, J., Sabbagh, U., Liang, Y., Olejnıkova, L., Dixon, K.G., Russell, A.L., Chen, J., Pan, Y.A., Triplett, J.W., and Fox, M.A. (2021). A cell-ECM mechanism for connecting the ipsilateral eye to the brain. Proc. Natl. Acad. Sci. U. S. A. *118*, 1–12.

Su, Y., Yuan, Y., Feng, S., Ma, S., and Wang, Y. (2017). High frequency stimulation induces sonic hedgehog release from hippocampal neurons. Sci. Rep. *7*, 1–13.

Tien, A.-C., Tsai, H.-H., Molofsky, A. V, McMahon, M., Foo, L.C., Kaul, A., Dougherty, J.D., Heintz, N., Gutmann, D.H., Barres, B.A., et al. (2012). Regulated temporal-spatial astrocyte precursor cell proliferation involves BRAF signalling in mammalian spinal cord. Development *139*, 2477–2487.

Tirou, L., Russo, M., Faure, H., Pellegrino, G., Demongin, C., Daynac, M., Sharif, A., Amosse, J., Le Lay, S., Denis, R., et al. (2021). Sonic Hedgehog receptor Patched deficiency in astrocytes enhances glucose metabolism in mice. Mol. Metab. *47*, 101172.

Traiffort, E., Moya, K.L., Faure, H., Hässig, R., and Ruat, M. (2001). High expression and anterograde axonal transport of aminoterminal sonic hedgehog in the adult hamster brain. Eur. J. Neurosci. *14*, 839–850.

Tran, N.M., Shekhar, K., Whitney, I.E., Jacobi, A., Benhar, I., Hong, G., Yan, W., Adiconis, X., Arnold, M.E., Lee, J.M., et al. (2019). Single-Cell Profiles of Retinal Ganglion Cells Differing in Resilience to Injury Reveal Neuroprotective Genes. Neuron *104*, 1039-1055.e12.

Tronche, F., Kellendonk, C., Kretz, O., Gass, P., Anlag, K., Orban, P.C., Bock, R., Klein, R., and Schütz, G. (1999). Disruption of the glucocorticoid receptor gene in the nervous system results in reduced anxiety. Nat. Genet. *23*, 99–103.

Ugbode, C.I., Smith, I., Whalley, B.J., Hirst, W.D., and Rattray, M. (2017). Sonic hedgehog signalling mediates astrocyte crosstalk with neurons to confer neuroprotection. J. Neurochem. *142*, 429–443.

Wallace, V.A., and Raff, M.C. (1999). A role for Sonic hedgehog in axon-to-astrocyte signalling in the rodent optic nerve. Development *126*, 2901–2909.

Wang, L., Klingeborn, M., Travis, A.M., Hao, Y., Arshavsky, V.Y., and Gospe, S.M. (2020). Progressive optic atrophy in a retinal ganglion cell-specific mouse model of complex I deficiency. Sci. Rep. *10*, 16326.

Wang, Y., Dakubo, G.D., Thurig, S., Mazerolle, C.J., and Wallace, V.A. (2005). Retinal ganglion cell-derived sonic hedgehog locally controls proliferation and the timing of RGC development in the embryonic mouse retina. Development *132*, 5103–5113.

Xu, Q., Wonders, C.P., and Anderson, S.A. (2005). Sonic hedgehog maintains the identity of cortical interneuron progenitors in the ventral telencephalon. Development *132*, 4987–4998.

Yabut, O.R., Ng, H.X., Yoon, K., Gomez, H.G., Arela, J.C., and Pleasure, S.J. (2019). Combined modulation of SHH and FGF signaling is crucial for maintenance of the neocortical progenitor specification program. BioRxiv *40*, 6872–6887.

Yuge, K., Kataoka, A., Yoshida, A.C., Itoh, D., Aggarwal, M., Mori, S., Blackshaw, S., and Shimogori, T. (2011). Region-specific gene expression in early postnatal mouse thalamus. J. Comp. Neurol. *519*, 544–561.

Zhang, Y., Narayan, S., Geiman, E., Lanuza, G.M., Velasquez, T., Shanks, B., Akay, T., Dyck, J., Pearson, K., Gosgnach, S., et al. (2008). V3 Spinal Neurons Establish a Robust and Balanced Locomotor Rhythm during Walking. Neuron *60*, 84–96.

Zimmerman, L., Lendahl, U., Cunningham, M., McKay, R., Parr, B., Gavin, B., Mann, J., Vassileva, G., and McMahon, A. (1994). Independent regulatory elements in the nestin gene direct transgene expression to neural stem cells or muscle precursors. Neuron *12*, 11–24.

FIGURE LEGENDS

Figure 1. Sonic hedgehog, but not retinal activity, is required for the recruitment of interneurons into visual thalamus

(A) Schematic representation of loss of retinal inputs and interneurons in visual thalamus of *Atoh7*$^{-/-}$ mice.

(B) ISH shows a reduction in *Gad1*$^{+}$ cells in dLGN and vLGN of >P150 *Atoh7*$^{-/-}$ mice compared with controls.

(C) Quantification of percentage of *Gad1*$^{+}$ cells in dLGN and vLGN of >P150 controls and *Atoh7*$^{-/-}$ mice. Each data point represents one biological replicate and bars depict means ± SEM. Asterisks (*) indicate $P < 0.05$ by Student's *t*-test (n=3 mice for each group).

(D) Schematic representation of *Calb2*^{Cre}-inducible expression of TeNT in RGCs. *Rosa26*$^{floxstop\text{-}TeNT}$ mice with the construct containing a *loxP*-flanked neomycin (Neo) cassette and TeNT coding sequence under *Rosa26* locus, were crossed with *Calb2*^{Cre} mice that harbor a *Cre* recombinase and internal ribosome entry site (IRES) in the *Calb2* locus.

(E) ISH for *Gad1* in dLGN and vLGN of P120 control and *Rosa26*$^{floxstop\text{-}TeNT}$*; Calb2*^{Cre} mice.

(F) Quantification revealed no significant difference in *Gad1*$^{+}$ cells in visual thalamus of control and *Rosa26*$^{floxstop\text{-}TeNT}$*;Calb2*^{Cre} mice. Each data point represents one biological replicate and bars depict means ± SEM. ns, indicates no significant differences by Student's *t*-test (n=3 mice for each group).

(G) Schematic representation of strategy to delete SHH from neural cells in the developing brain. This was achieved by crossing *Shh*$^{fl/fl}$ mice, which have two *loxP* sites flanking exon 2 of the *Shh* gene, with *Nes*^{Cre} transgenic mice that contain a *Cre* recombinase and human growth hormone polyadenylation signal (hGH pA) under the control of *Nestin* promoter and enhancer.

(H) ISH revealed a dramatic reduction in *Gad1*$^{+}$ cells in dLGN and vLGN of P18 *Shh*$^{fl/fl}$*Nes*^{Cre} mice compared with controls.

(I) Quantification of percentage of *Gad1*$^{+}$ cells in dLGN and vLGN of P18 control and *Shh*$^{fl/fl}$*Nes*^{Cre} mice. Each data point represents one biological replicate and bars depict means ± SEM. Asterisks represent significant differences (***$P < 0.001$; *$P < 0.05$) by Student's *t*-test (n=3 mice for each group).

Scale bars in C, E, H: 100 µm.

Figure 2. Expression of SHH signaling molecules by astrocytes in visual thalamus

(A) Raw transcript reads of mRNAs for downstream SHH signaling components in P3 dLGN and vLGN by RNAseq. Each data point represents a different biological replicate and bars depict means ± SEM.

(B) Presence of *Gli1-tdT*$^{+}$ cells in dLGN and vLGN of P7 *Rosa26*^{tdT}*;Gli1*^{CreER} mice.

(C) IHC for S100ß in P7 *Rosa26*^{tdT}*;Gli1*^{CreER} mice revealed S100ß expression in *Gli1-tdT*$^{+}$ cells in visual thalamus.

(E) Quantification of percentage of *Gli1-tdT*$^{+}$ cells that express S100ß in P7 visual thalamus. Each data point represents one biological replicate and bars depict means ± SEM (n=3 mice for each region).

(D) ISH for *Gja1* in P7 *Rosa26*^{tdT}*;Gli1*^{CreER} mice revealed expression of *Gja1* mRNA by *Gli1-tdT*$^{+}$ cells in visual thalamus.

(F) Quantification shows 100% of *Gli1-tdT*$^{+}$ cells express the astrocytic marker *Gja1* in P7 visual thalamus. Each data point represents one biological replicate and bars depict means ± SEM (n=3 mice for each region).

(G) RNAscope-based ISH detected *Ptch1* mRNA in dLGN and vLGN of P3 *Aldh1l1-GFP* mice. This revealed expression of *Ptch1* mRNA in the cell bodies as well as in the processes of *Aldh1l1-GFP*$^{+}$ astrocytes.

(H) Quantification of percentage of *Aldh1l1-GFP*$^{+}$ astrocytes that express *Ptch1* mRNA in P3 visual thalamus. Each data point represents one biological replicate and bars depict means ± SEM (n=3 mice for each region).

(I) RNAscope-based ISH detected *Smo* mRNA in dLGN and vLGN of P3 *Aldh1l1-GFP* mice. This revealed expression of *Smo* mRNA in the cell bodies as well as in the processes of *Aldh1l1-GFP*$^{+}$ astrocytes.

(J) Quantification of percentage of *Aldh1l1-GFP*$^{+}$ astrocytes that express *Smo* mRNA in P3 visual thalamus. Each data point represents one biological replicate and bars depict means ± SEM (n=3 mice for each region).

Scale bars in B: 200 µm and in C, E, G, I: 10 µm.

Figure 3. Deletion of SHH from RGCs in the perinatal retina

(A) RNAscope-based ISH revealed dense *Shh* mRNA in the GCL of P3 retina (inner nuclear layer, INL; inner plexiform layer, IPL; ganglion cell layer, GCL).

(B) RNAscope-based ISH revealed *Shh* mRNA in CALB2^{+} cells in the GCL of P3 retina.

(C) Single-cell RNAseq data (from Rheaume et al., 2018) analyzed to show *Calb2* and *Shh* mRNA expression by different subtypes of RGCs in P5 mouse retina.

(D) Single-cell RNAseq data (from Shekhar et al., 2022) analysis for developmental expression of *Calb2* by RGCs.

(E) qRT-PCR showed a reduction in *Shh* mRNA in retina of P3 *Shh*$^{fl/fl}$;*Calb2*^{Cre} mice compared to controls. Each data point represents one biological replicate and bars depict means ± SEM. Asterisks (*) indicate $P < 0.05$ by Student's *t*-test (n=3 mice for each group).

Scale bars in A: 100 µm and in B: 10 µm.

Figure 4. Retinal innervations innervate visual thalamus in the absence of RGC-derived SHH

(A) CTB-labeled eye-specific retinal projections to dLGN in P25 control and P25 *Shh*$^{fl/fl}$;*Calb2*^{Cre} mutant mice.

(B) Quantification for the percentage of dLGN area covered by contraRGCs projections, ipsiRGCs projections, or overlapping eye-specific projections in controls and *Shh*$^{fl/fl}$;*Calb2*^{Cre} mutants. Each data point represents one biological replicate and bars depict means ± SEM. ns, indicates no significant differences by Student's t-test (n=3 mice for each group).

Scale bar in A: 100 µm.

Figure 5. Absence of RGC-derived SHH does not impact astrocyte distribution but decreases *Fgf15* expression in the visual thalamus

(A) ISH revealed reduced *Fgf15* expression in dLGN and vLGN of P3 *Shh*$^{fl/fl}$;*Calb2*^{Cre} mutants compared to controls.

(B) Quantification for density of *Fgf15*$^{+}$ cells in dLGN and vLGN of P3 control and *Shh*$^{fl/fl}$;*Calb2*^{Cre} mutant mice. Each data point represents one biological replicate and bars depict means ± SEM. Asterisks (*) indicate $*P < 0.05$ by Student's *t*-test (n=3 mice for each group).

(C) ISH revealed no change in *Fgfr3*$^{+}$ astrocytes in dLGN and vLGN of P7 *Shh*$^{fl/fl}$;*Calb2*^{Cre} mutants compared to controls.

(D) Quantification for density of *Fgfr3*$^{+}$ cells in dLGN and vLGN of P7 control and *Shh*$^{fl/fl}$;*Calb2*^{Cre} mutant mice. Each data point represents one biological replicate and bars depict means ± SEM. ns, indicates no significant differences by Student's t-test (n=3 mice for each group).

Scale bars in A, C: 100 µm.

Figure 6. RGC-derived SHH is required for the recruitment of *Gad1*$^{+}$ interneurons into visual thalamus

(A) ISH revealed a reduction in *Gad1*$^{+}$ cells in dLGN and vLGN of P7 *Shh*$^{fl/fl}$;*Calb2*^{Cre} mutants compared with controls.

(B) Quantification of percentage of *Gad1*$^{+}$ cells in dLGN and vLGN of P7 *Shh*$^{fl/fl}$;*Calb2*^{Cre} and control mice. Each data point represents one biological replicate and bars depict means ± SEM. Asterisks (*) indicate *$P < 0.05$ by Student's *t*-test (n=3 mice for each group).

(C) ISH revealed a reduction in *Gad1*$^{+}$ cells in dLGN and vLGN of >P90 *Shh*$^{fl/fl}$;*Calb2*^{Cre} mutants compared with controls.

(D) Quantification of percentage of *Gad1*$^{+}$ cells in dLGN and vLGN of adult *Shh*$^{fl/fl}$;*Calb2*^{Cre} and control mice. Each data point represents one biological replicate and bars depict means ± SEM. Asterisks (*) indicate *$P < 0.05$ by Student's *t*-test (n=4 mice for control dLGN group, n=3 mice for mutant dLGN group, n=6 mice for control vLGN group, and n=5 mice for mutant vLGN group).

Scale bars in A, C: 100 µm.

Figure 1—figure supplement 1. Thalamic *Fgf15* expression is dependent on retinal inputs and SHH

(A) ISH revealed a dramatic reduction in *Fgf15* expression in dLGN and vLGN of P2 *Atoh7*$^{-/-}$ mutants compared with controls.

(B) ISH revealed a dramatic reduction in *Fgf15* expression in dLGN and vLGN of P3 *Shh*$^{fl/fl}$*Nes*^{Cre} mutants compared with controls.

(C) Quantification for density of *Fgf15*$^{+}$ cells in dLGN and vLGN of P3 control and *Shh*$^{fl/fl}$*Nes*^{Cre} mutant mice. Each data point represents one biological replicate and bars depict means ± SEM. Asterisks (*) indicate $*P < 0.05$ by Student's *t*-test

Scale bars in A, B: 100 μm.

Figure 1—figure supplement 2. Anatomical and functional characterization of *Rosa26$^{floxstop\text{-}TeNT}$;Calb2^{Cre}* mice

(A) Expression of tdT in the GCL of P0 *Rosa$^{stop\text{-}tdT}$;Calb2^{Cre}* mouse retina.

(B) Schematic representation of the behavioral response to a looming visual stimulus.

(C) Adult *Rosa26$^{floxstop\text{-}TeNT}$;Calb2^{Cre}* (age-matched and littermate mutants to controls) and *Atoh7$^{-/-}$* mutants (not age-matched and not littermate mutants to controls) had reduced reaction times to a looming visual stimulus compared with controls. Each data point represents one biological replicate and bars depict means ± SEM. Asterisks represent significant differences (***$P < 0.001$; *$P < 0.05$) by Student's *t*-test.

(D) CTB-labeled eye-specific retinal projections to dLGN in P16 control and P24 *Rosa26$^{floxstop\text{-}TeNT}$;Calb2^{Cre}* mutant mice.

(E) Quantification of the percentage of dLGN area covered by contraRGCs projections, ipsiRGCs projections, or overlapping eye-specific projections in controls and *Rosa26$^{floxstop\text{-}TeNT}$;Calb2^{Cre}* mutants. Each data point represents one biological replicate and bars depict means ± SEM. Asterisks (*) indicate *$P < 0.05$ by Student's *t*-test (n=7 mice for control group and n=8 mice for mutant group).

Scale bars in A: 50 µm and D: 200 µm.

Figure 3—figure supplement 1. Presence of active SHH signaling in developing visual thalamus

(A) Bright-field immunohistochemistry for βGal in dLGN and vLGN of P3 *Gli1*$^{nlacZ/+}$ mice.

Scale bar in A: 100 μm.

Figure 3—figure supplement 2. Expression of CALB2 in developing LGN and interneuron progenitor zones

(A) IHC for CALB2 shows sparse expression in P3 tectal and thalamic progenitor zones of thalamic GABAergic interneurons.

Scale bar in A: 100 µm.

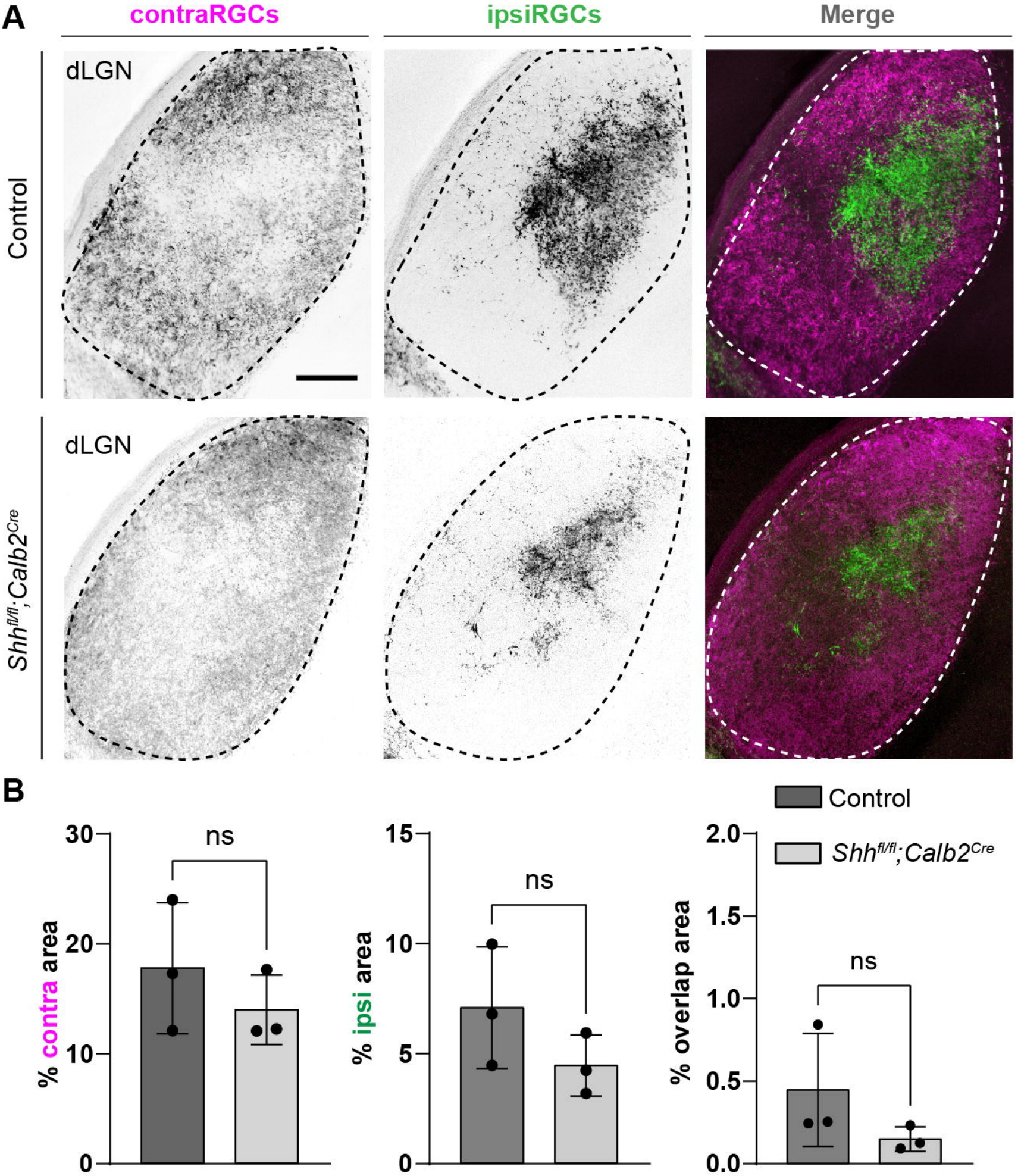
A
contraRGCs
ipsiRGCs
Merge
Control
dLGN
dLGN
Shh^fl/fl;Calb2^Cre
B
Control
Shh^fl/fl;Calb2^Cre
% contra area
% ipsi area
% overlap area
ns
ns
ns
30
20
10
0
15
10
5
0
2.0
1.5
1.0
0.5
0.0

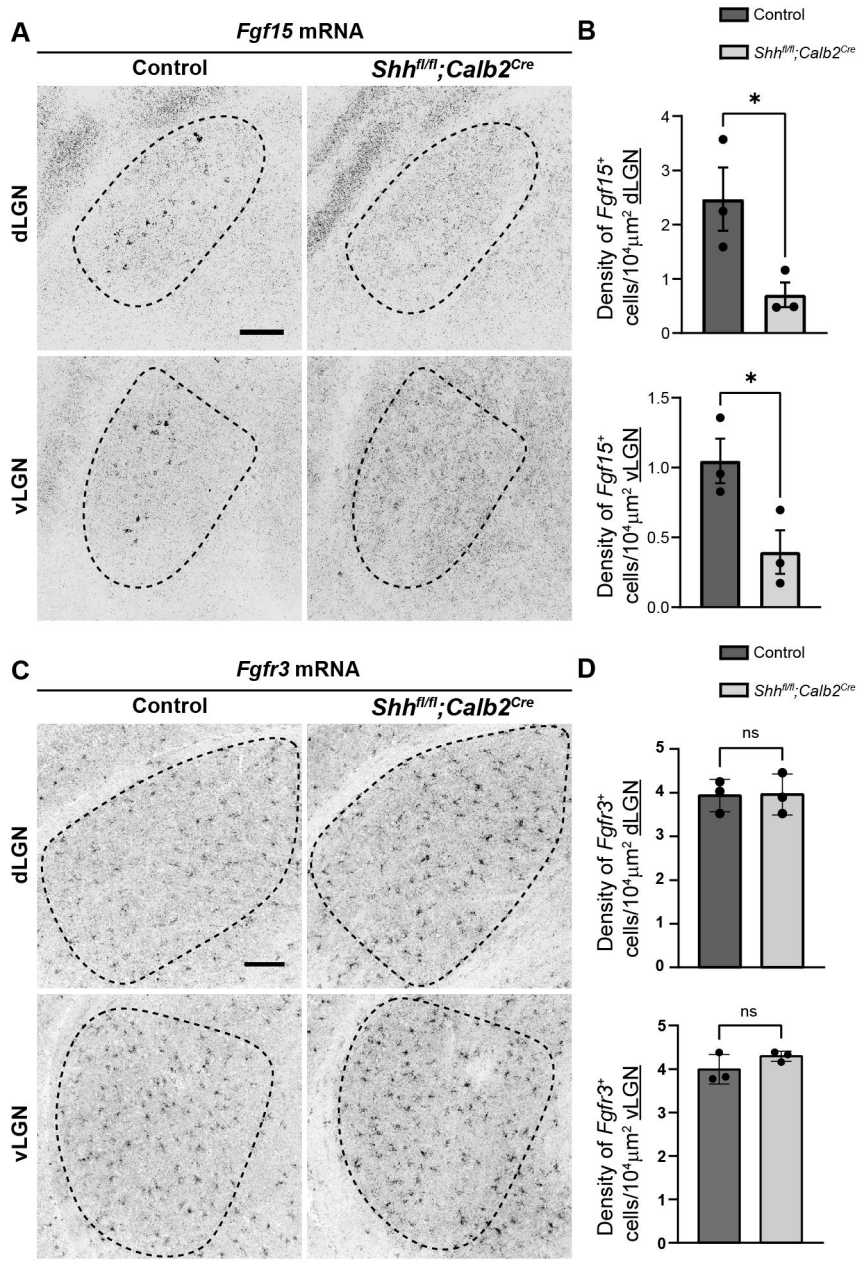
A
Fgf15 mRNA
Control
Shh^fl/fl;Calb2^Cre
dLGN
vLGN
B
Control
Shh^fl/fl;Calb2^Cre
Density of Fgf15+ cells/10^4μm^2 dLGN
Density of Fgf15+ cells/10^4μm^2 vLGN
*
C
Fgfr3 mRNA
Control
Shh^fl/fl;Calb2^Cre
dLGN
vLGN
D
Control
Shh^fl/fl;Calb2^Cre
Density of Fgfr3+ cells/10^4μm^2 dLGN
Density of Fgfr3+ cells/10^4μm^2 vLGN
ns

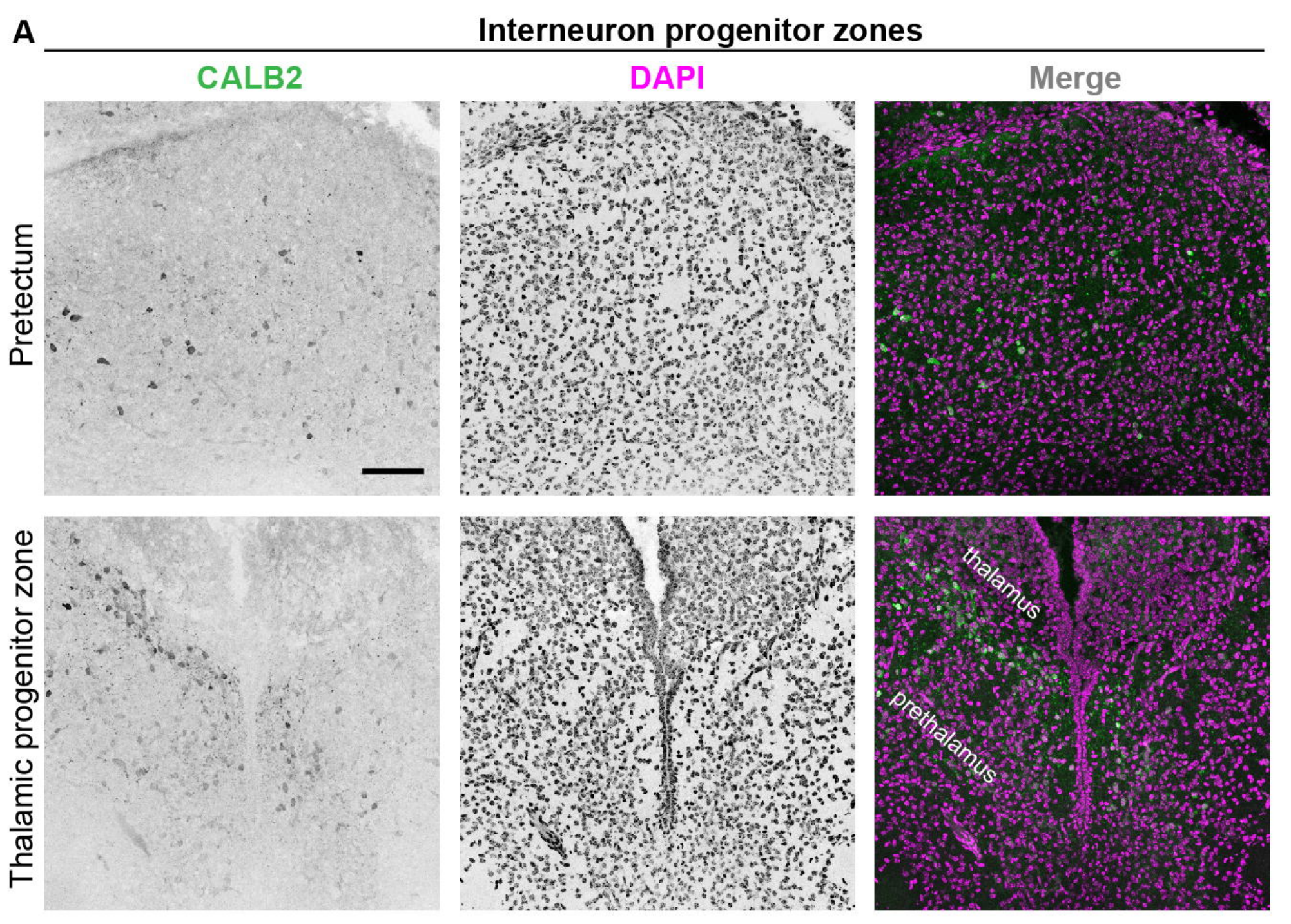
A
Interneuron progenitor zones
CALB2
DAPI
Merge
Pretectum
Thalamic progenitor zone
thalamus
prethalamus

A

Gli1$^{nlacZ/+}$

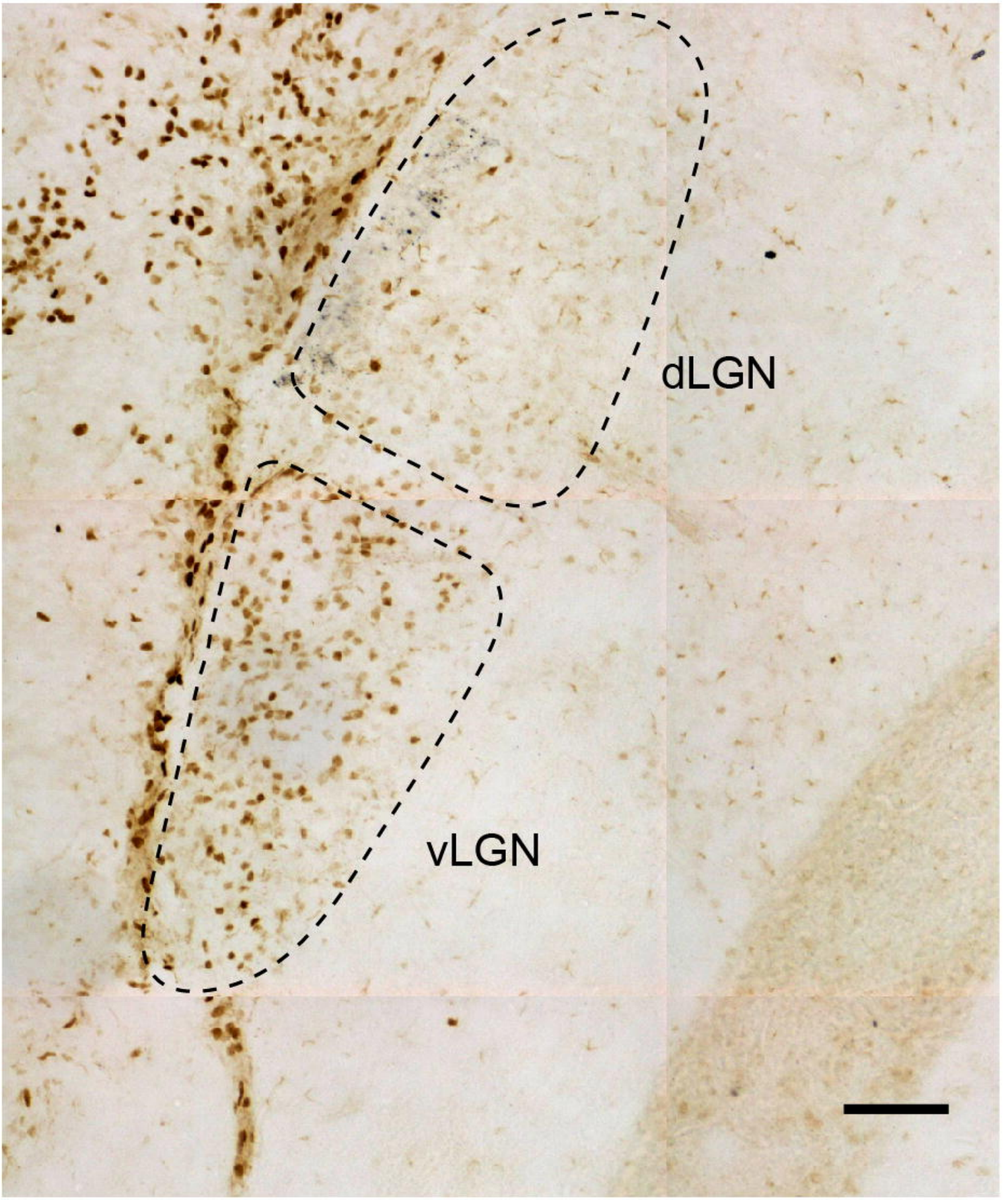

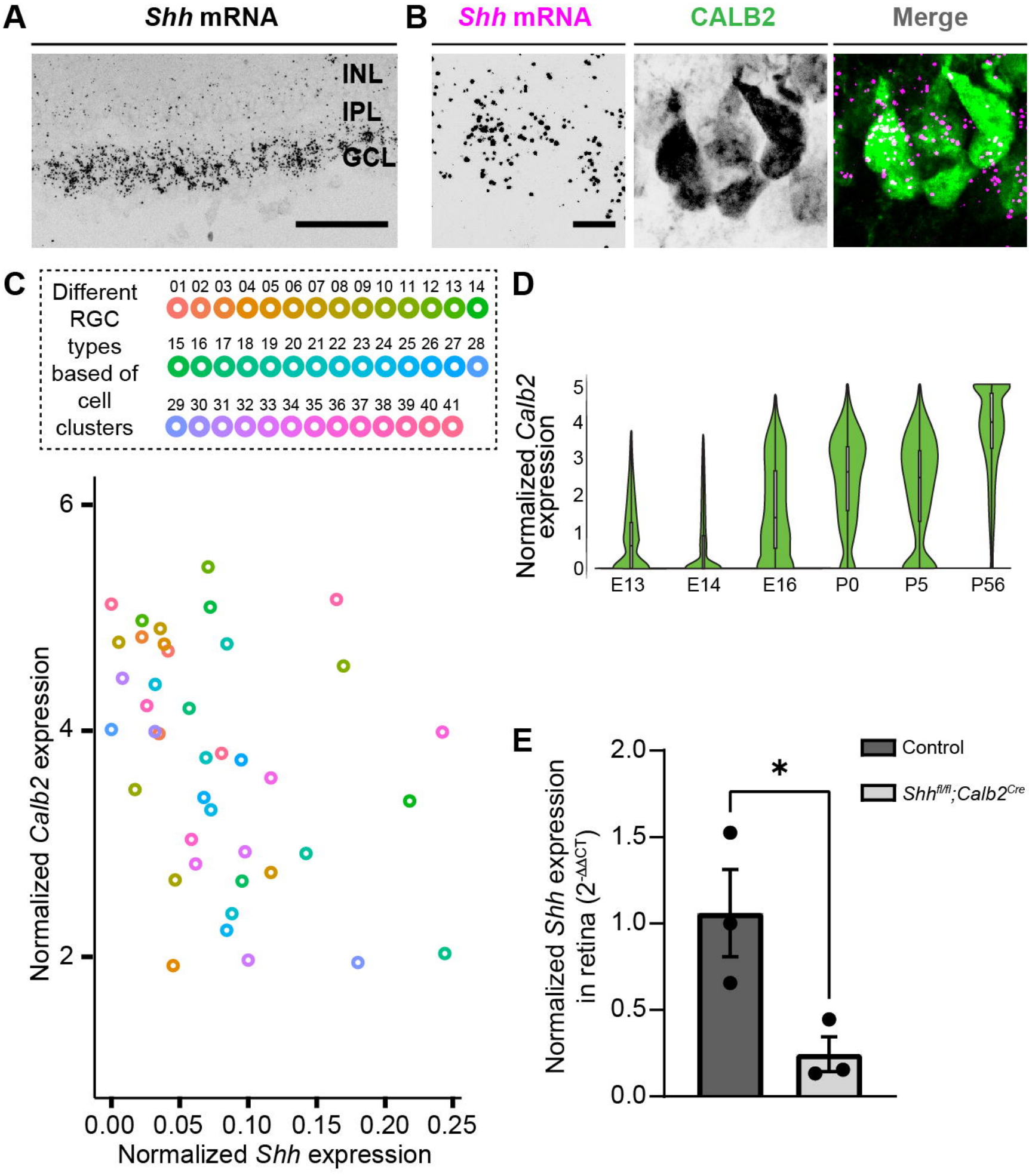
A
Shh mRNA
INL
IPL
GCL
B
Shh mRNA
CALB2
Merge
C
Different RGC types based of cell clusters
01 02 03 04 05 06 07 08 09 10 11 12 13 14
15 16 17 18 19 20 21 22 23 24 25 26 27 28
29 30 31 32 33 34 35 36 37 38 39 40 41
Normalized Calb2 expression
Normalized Shh expression
0.00 0.05 0.10 0.15 0.20 0.25
2
4
6
D
Normalized Calb2 expression
0
1
2
3
4
5
E13
E14
E16
P0
P5
P56
E
Normalized Shh expression in retina (2^-ΔΔCT)
0.0
0.5
1.0
1.5
2.0
*
Control
Shh^fl/fl;Calb2^Cre

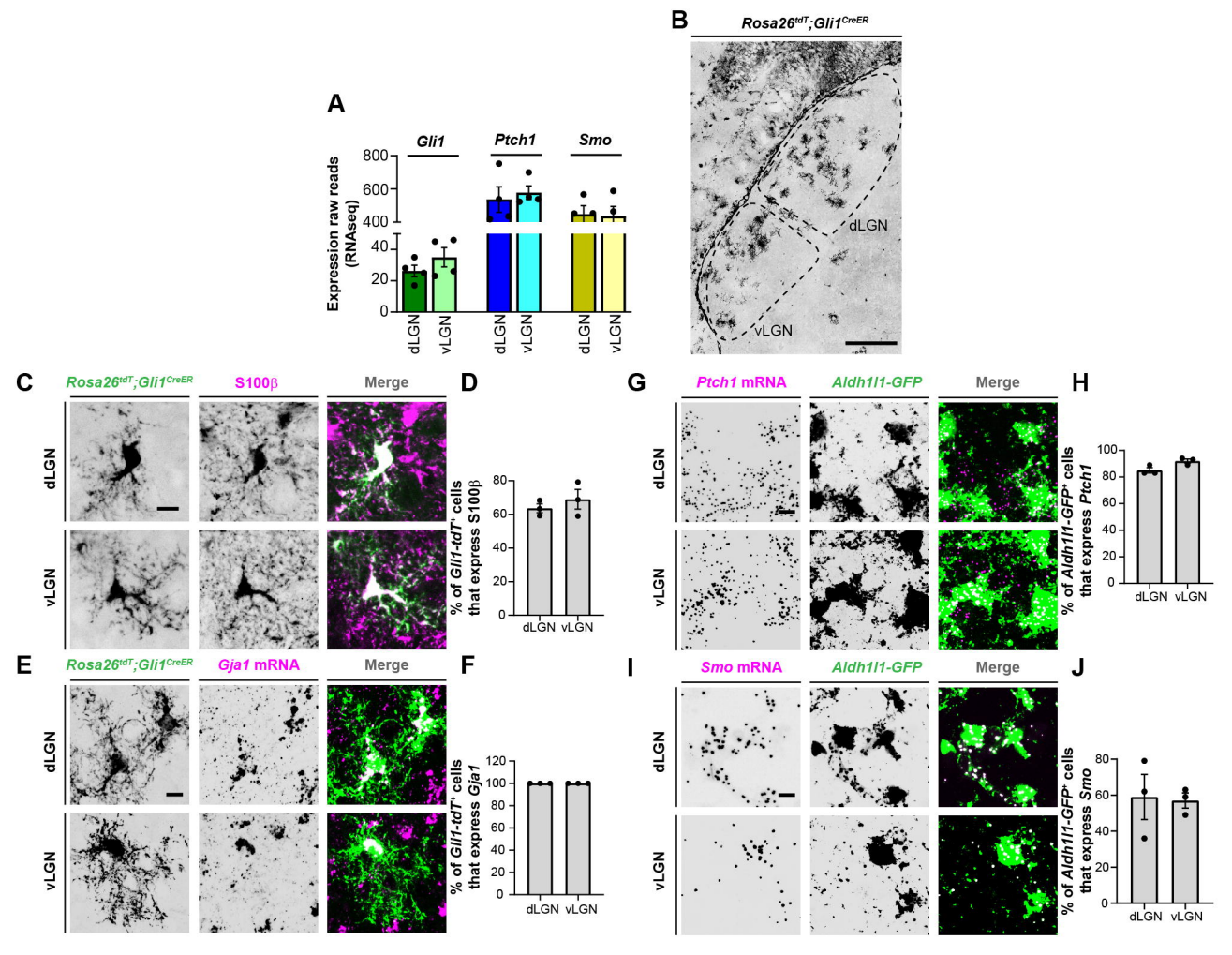
A
Gli1
Ptch1
Smo
Expression raw reads (RNAseq)
800
600
400
40
20
0
dLGN
vLGN
B
Rosa26tdT;Gli1CreER
dLGN
vLGN
C
Rosa26tdT;Gli1CreER
S100β
Merge
D
% of Gli1-tdT+ cells that express S100β
E
Rosa26tdT;Gli1CreER
Gja1 mRNA
Merge
F
% of Gli1-tdT+ cells that express Gja1
G
Ptch1 mRNA
Aldh1l1-GFP
Merge
H
% of Aldh1l1-GFP+ cells that express Ptch1
I
Smo mRNA
Aldh1l1-GFP
Merge
J
% of Aldh1l1-GFP+ cells that express Smo

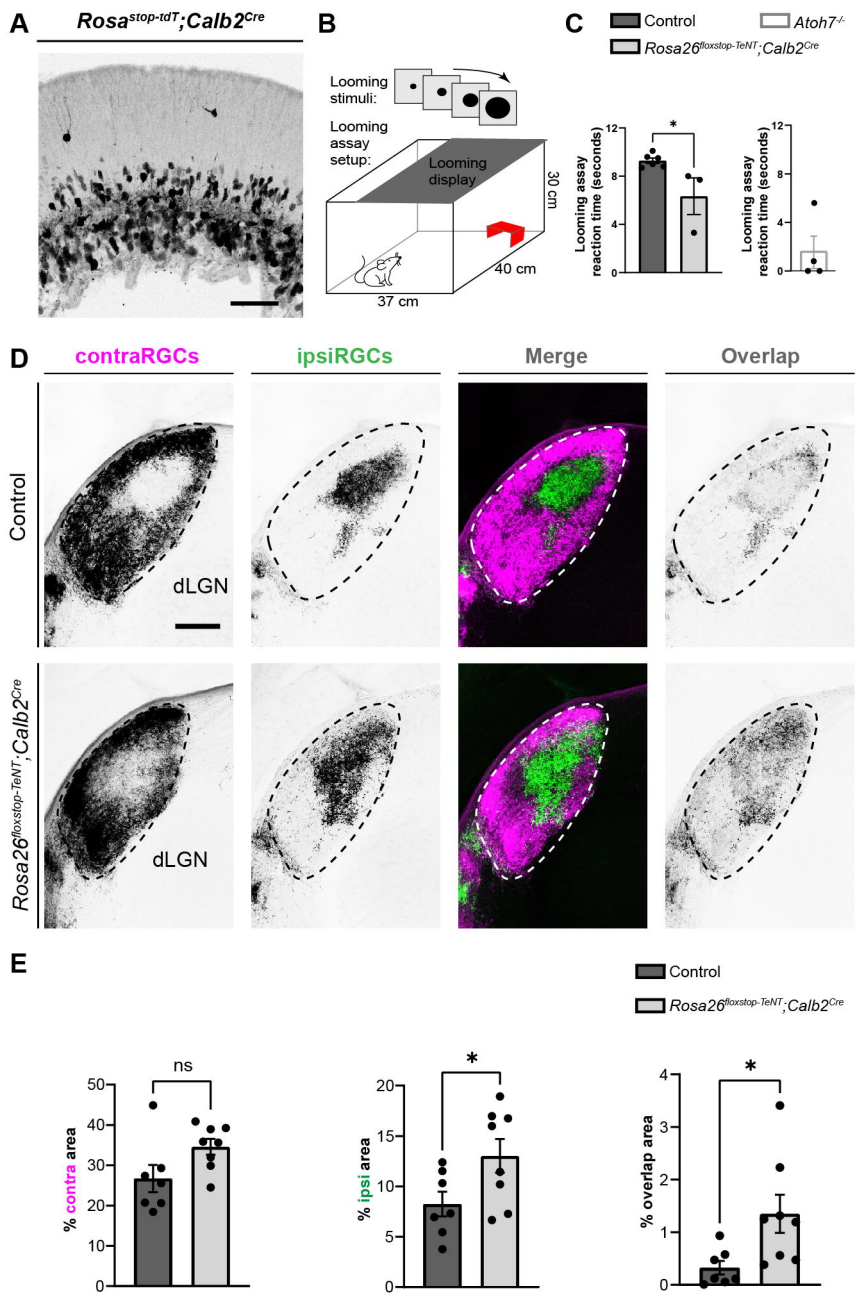
A
Rosa^stop-tdT;Calb2^Cre
B
Looming stimuli:
Looming assay setup:
Looming display
30 cm
40 cm
37 cm
C
Control
Atoh7-/-
Rosa26^floxstop-TeNT;Calb2^Cre
Looming assay reaction time (seconds)
*
D
contraRGCs
ipsiRGCs
Merge
Overlap
Control
Rosa26^floxstop-TeNT;Calb2^Cre
dLGN
E
Control
Rosa26^floxstop-TeNT;Calb2^Cre
ns
% contra area
% ipsi area
% overlap area

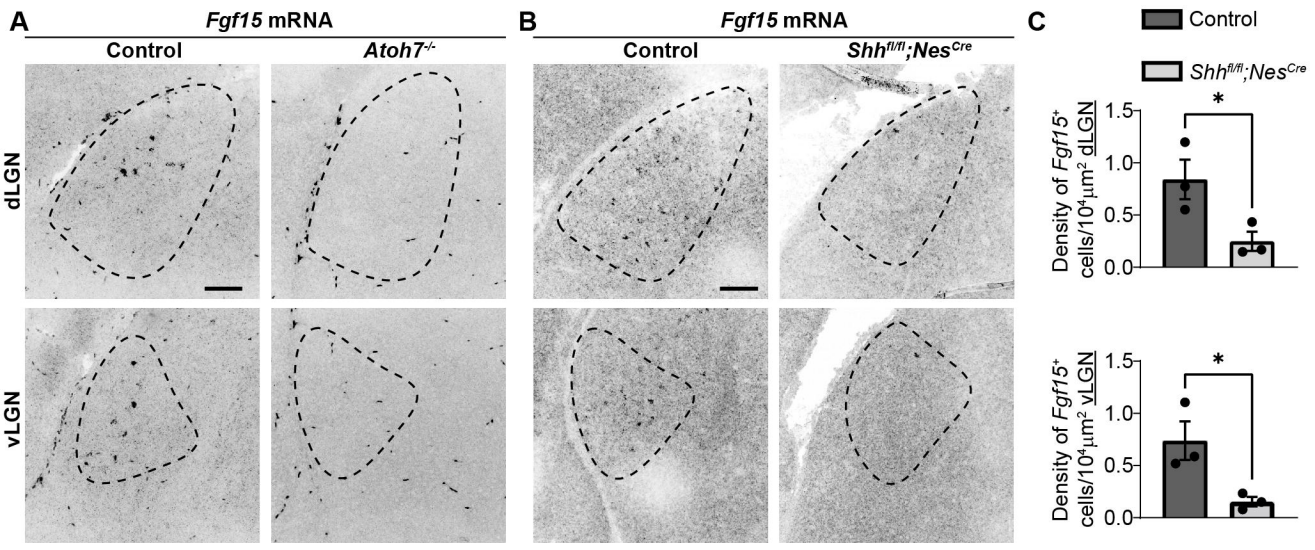
A
Fgf15 mRNA
Control
Atoh7-/-
dLGN
vLGN
B
Fgf15 mRNA
Control
Shhfl/fl;NesCre
C
Control
Shhfl/fl;NesCre
Density of Fgf15+ cells/10⁴µm² dLGN
Density of Fgf15+ cells/10⁴µm² vLGN
1.5
1.0
0.5
0.0
*

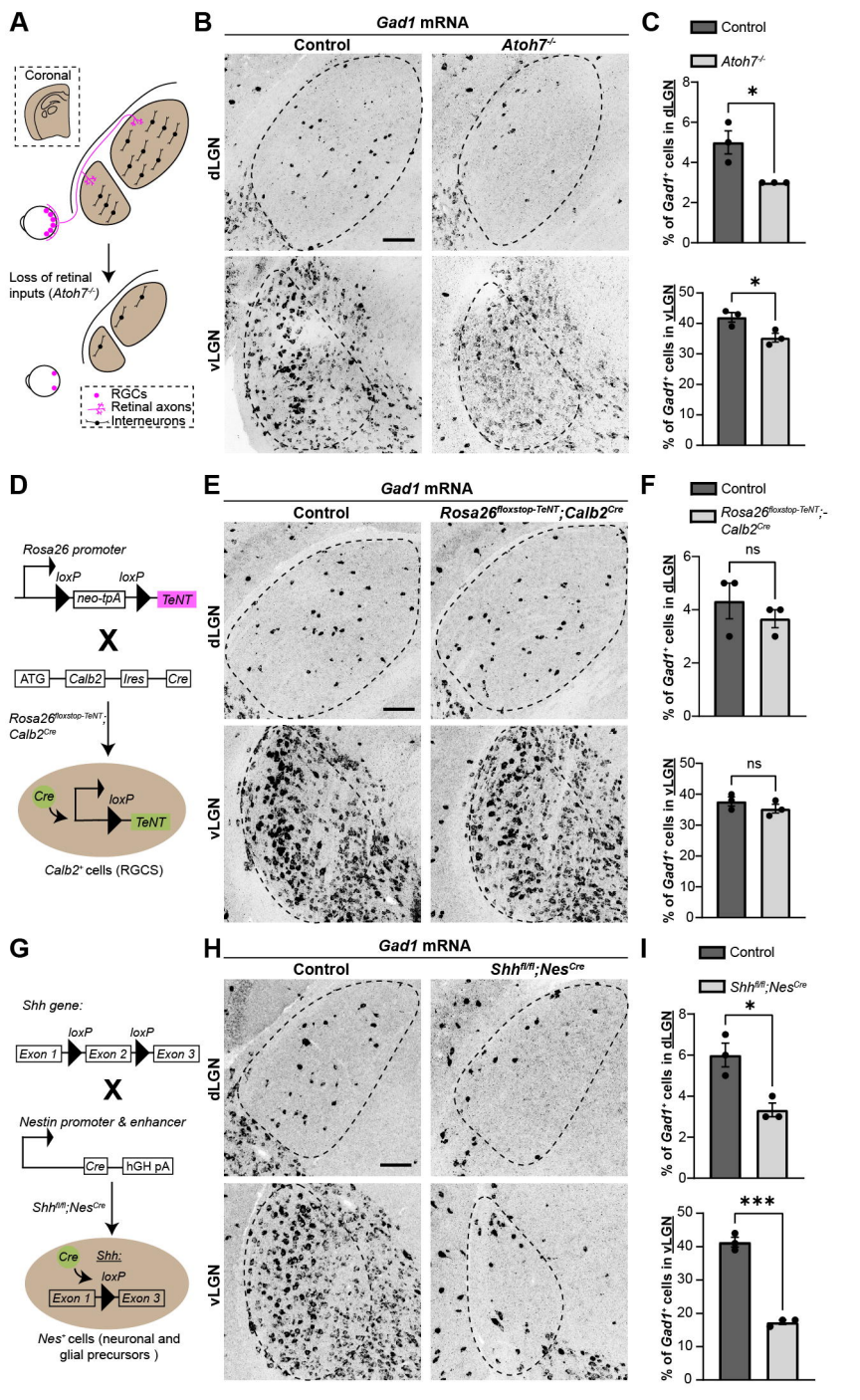
A
Coronal
Loss of retinal inputs (Atoh7-/-)
RGCs
Retinal axons
Interneurons
B
Gad1 mRNA
Control
Atoh7-/-
dLGN
vLGN
C
Control
Atoh7-/-
% of Gad1+ cells in dLGN
% of Gad1+ cells in vLGN
D
Rosa26 promoter
loxP
loxP
neo-tpA
TeNT
X
ATG
Calb2
Ires
Cre
Rosa26floxstop-TeNT;Calb2Cre
Cre
loxP
TeNT
Calb2+ cells (RGCS)
E
Gad1 mRNA
Control
Rosa26floxstop-TeNT;Calb2Cre
dLGN
vLGN
F
Control
Rosa26floxstop-TeNT;-Calb2Cre
ns
% of Gad1+ cells in dLGN
% of Gad1+ cells in vLGN
G
Shh gene:
loxP
loxP
Exon 1
Exon 2
Exon 3
X
Nestin promoter & enhancer
Cre
hGH pA
Shhfl/fl;NesCre
Cre
Shh:
loxP
Exon 1
Exon 3
Nes+ cells (neuronal and glial precursors)
H
Gad1 mRNA
Control
Shhfl/fl;NesCre
dLGN
vLGN
I
Control
Shhfl/fl;NesCre
% of Gad1+ cells in dLGN
% of Gad1+ cells in vLGN

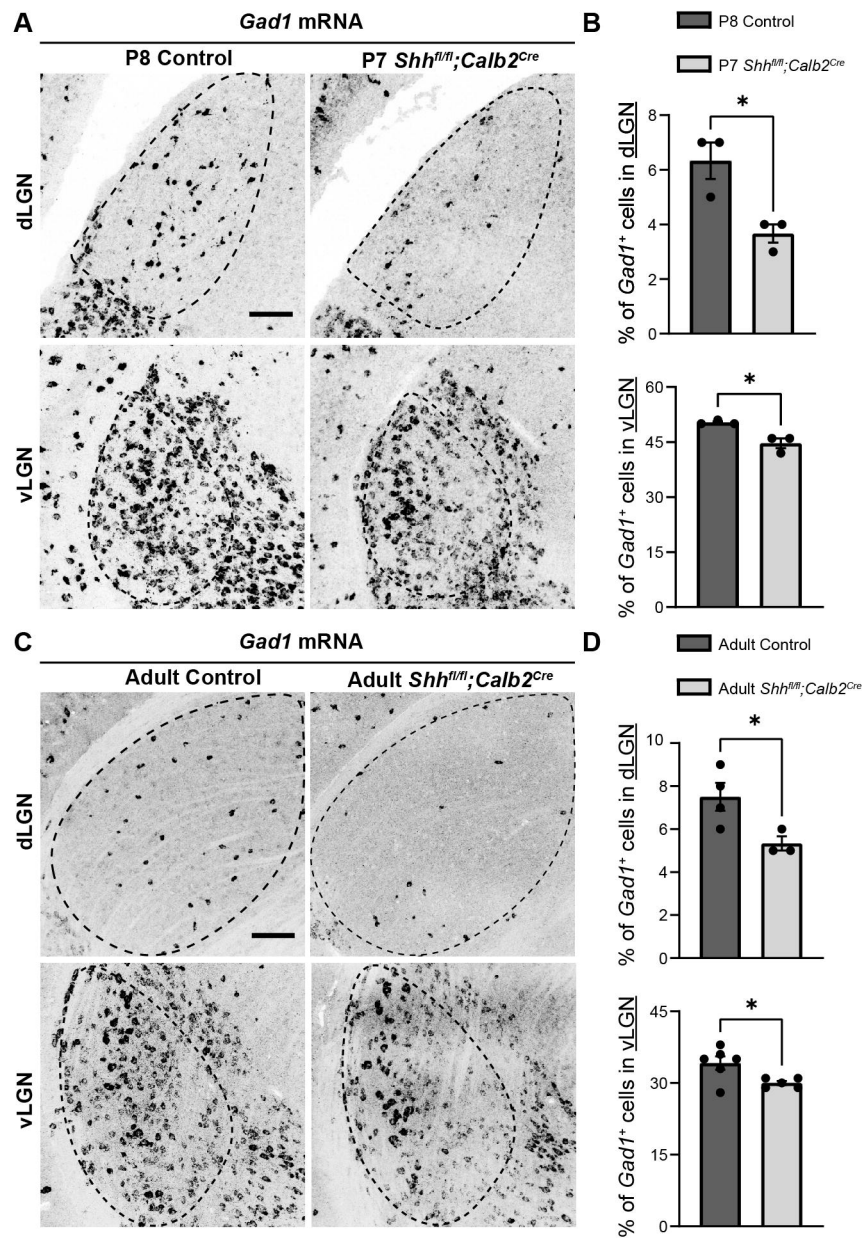
A
Gad1 mRNA
P8 Control
P7 Shhfl/fl;Calb2Cre
dLGN
vLGN
B
P8 Control
P7 Shhfl/fl;Calb2Cre
% of Gad1+ cells in dLGN
% of Gad1+ cells in vLGN
C
Gad1 mRNA
Adult Control
Adult Shhfl/fl;Calb2Cre
dLGN
vLGN
D
Adult Control
Adult Shhfl/fl;Calb2Cre
% of Gad1+ cells in dLGN
% of Gad1+ cells in vLGN